4 ANL Test Results

4.1 Crack Growth Data

This section presents the crack growth data obtained from five 1-T CT specimens. Two of these specimens, CT31-W01 TS and CT31-W02 TS, were cut from a double-J weld, while the remaining three, CT933-TS, CT933-TL, and CT933-LS, were machined from a deep-groove weld.

4.1.1 Crack Growth Data for Double-J Weld Specimen CT31-W01 TS

The CGR test on Specimen CT31–W01 TS of Alloy 182 SMA weld was conducted in simulated PWR water at 320°C, in recirculating mode at a flow rate of ≈60 cc/min. The environmental conditions stabilized after about a week. The ECPs, measured at 289°C at the exit of the autoclave, of a Alloy 600 sample and Pt electrode were –686 and –690 mV (SHE), respectively; the water system was switched to the once–through mode during ECP measurements to prevent possible contamination of the test solution. The specimen was fatigue precracked at R = 0.3, K_{max} = 23 MPa m$^{1/2}$, triangular waveform, and 0.5 Hz frequency. After ≈0.3–mm extension, R was increased incrementally to 0.7 and the frequency decreased to 0.005 Hz. The experimental conditions and results for the test are given in Table 5; the changes in crack length and K_{max} with time during various test periods are shown in Fig. 27. Note that at 140, 250, 380, and 580 h, the DC potential measurements were not recorded for short periods extending 10–20 h.

The test was interrupted at 407 h and 593 h because of large fluctuations in the system pressure. The problem was identified to be caused by $Al(OH)_3$ deposits in the cooler regions of the water system. Alumina beads used to insulate the DC potential and current leads were the source for Al. In the recirculating system, the concentration of Al gradually built up during operation, eventually leading to plugging of the high pressure letdown line. The entire return line from the autoclave to the supply feedwater tank, including the back–pressure regulator, was replaced or cleaned by back flushing. The test was restarted under the loading conditions prior to the interruption, but the system was operated in a once–through mode at a lower flow rate of ≈10 cc/min. In the case of both interruptions, the CGRs existing before the interruption were restored after restart.

Table 5. Crack growth data for specimen CT31-W01 TS of Alloy 182 SMA weld in PWR water[a] at 320°C.

| Test Period	Test Time, h	Conduc- tivity,[b] μS/cm	O$_2$ Conc.,[b] ppb	Load Ratio R	Rise Time, s	Down Time, s	Hold Time, s	K_{max}, MPa·m$^{1/2}$	ΔK, MPa·m$^{1/2}$	CGR$_{env}$, m/s	Estimated CGR$_{air}$, m/s	Crack Length, mm
1	25	25.0	<10	0.3	1	1	0	23.22	16.25	5.62E-08	1.55E-08	12.976
2	40	25.0	<10	0.3	10	10	0	24.00	16.80	1.72E-08	1.78E-09	13.523
3	90	25.0	<10	0.6	10	10	0	23.86	9.55	1.94E-09	4.17E-10	13.718
4a	135	25.3	<10	0.7	10	10	0	24.64	7.39	1.59E-09	2.15E-10	13.832
4b	281	25.3	<10	0.7	10	10	0	25.26	7.58	1.26E-09	2.38E-10	14.371
5	407	24.4	<10	0.7	100	100	0	25.43	7.63	2.55E-10	2.45E-11	14.394
6	498	23.9	<10	0.7	100	100	0	25.59	7.68	2.73E-10	2.52E-11	14.497
7	552	22.7	<10	0.7	500	500	0	25.57	7.67	negligible	5.02E-12	14.497
8	593	23.0	<10	0.7	1000	12	0	28.55	8.56	2.40E-10	3.94E-12	14.588
9	858	20.0	<10	0.7	1000	12	0	28.86	8.66	5.25E-11	4.12E-12	14.687
10	1214	20.5	<10	0.7	1000	12	3600	29.03	8.71	9.79E-11[c]	4.22E-12	14.790

[a]Simulated PWR water with 2 ppm Li, 1100 ppm B, and 2 ppm dissolved hydrogen (≈23 cc/kg).
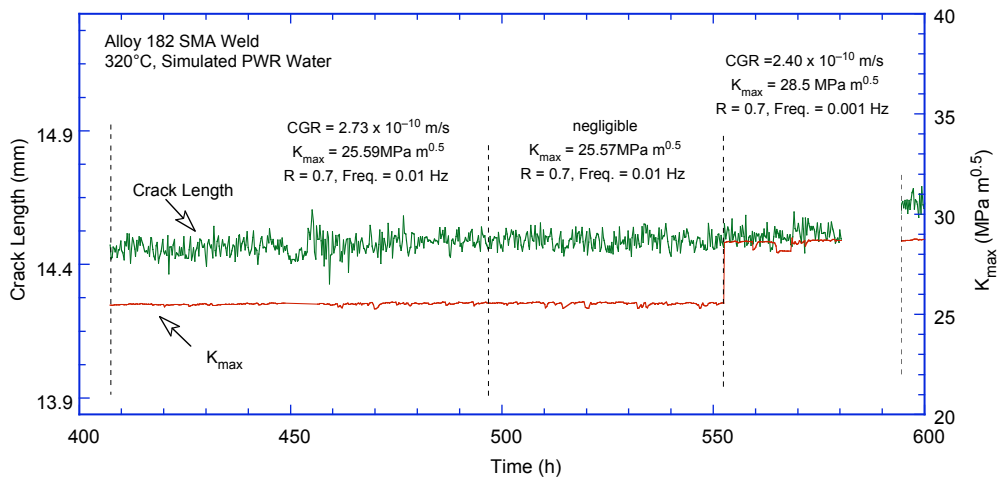[b]Represents values in the effluent; conductivity was ≈21.5 μS/cm in feedwater.
[c]Represents the SCC component of the CGR.
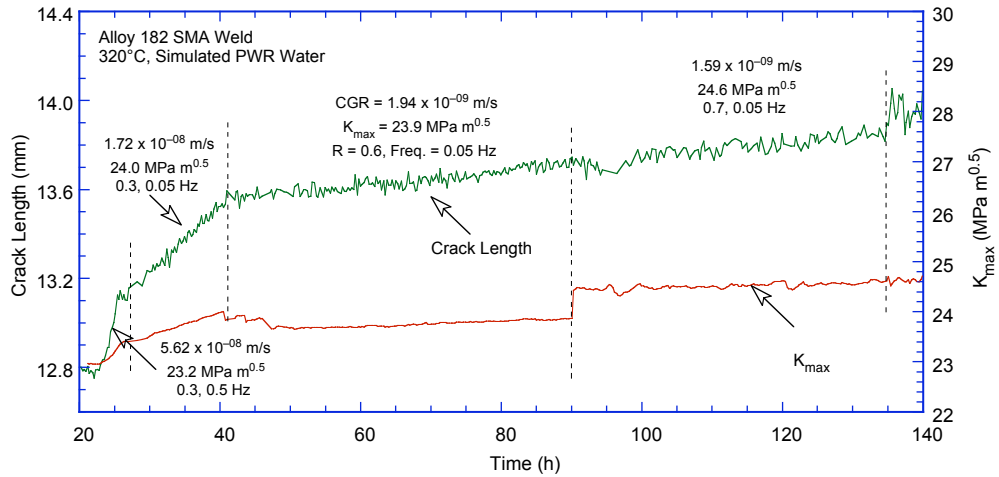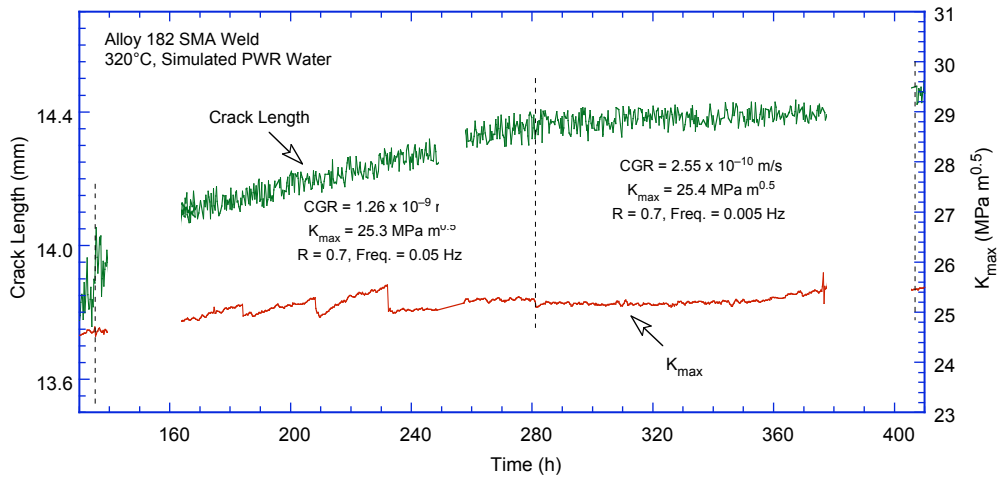
Figure 27. Crack length vs. time for Alloy 182 SMA weld–metal specimen CT31-W01 TS in simulated PWR environment at 320°C during test periods (a) 1–4a, (b) 4b–5, (c) 6–8, (d) 9, and (e) 10.
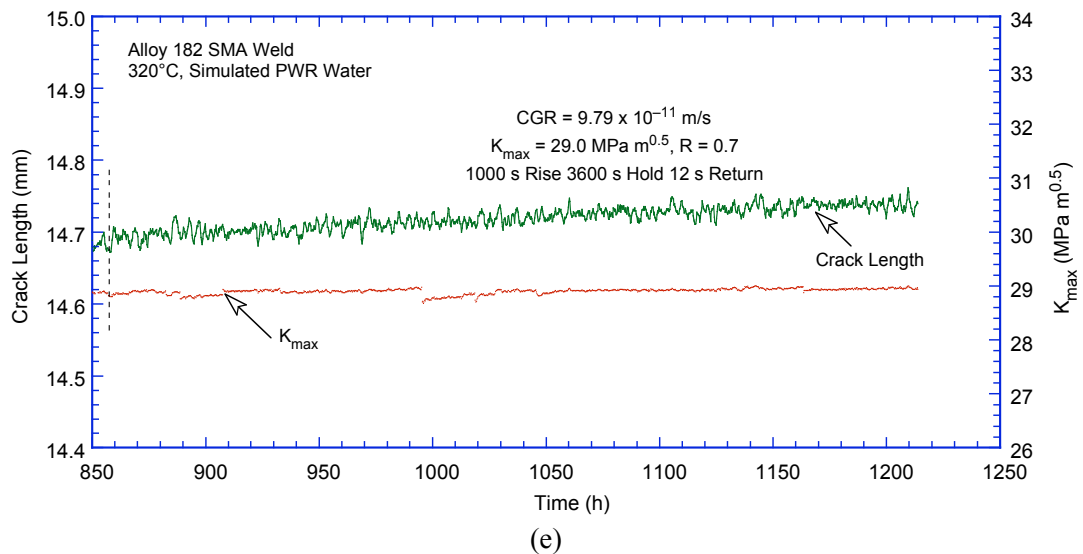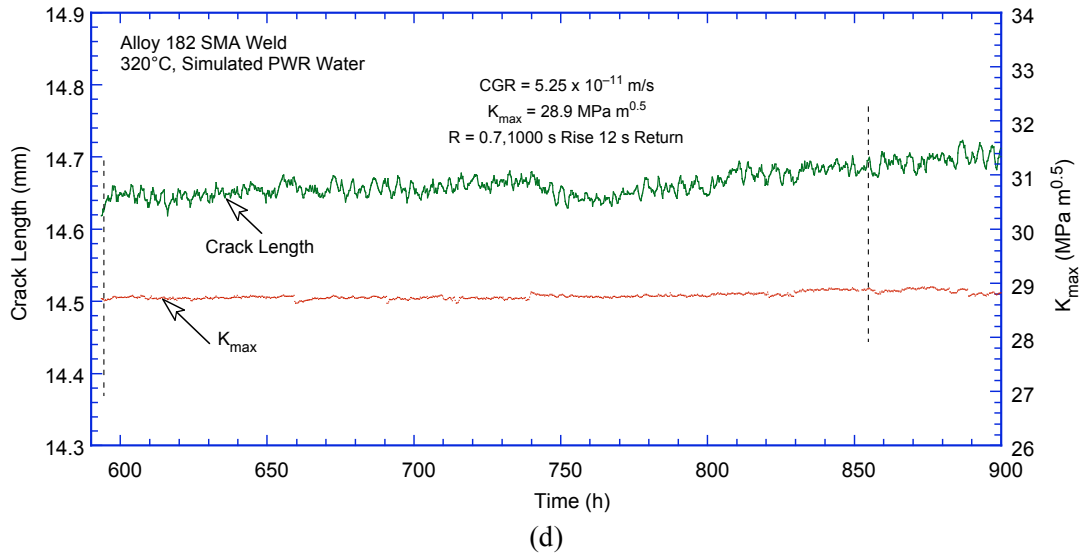
Figure 27. (Contd.)

After the test, the specimen was fractured in liquid nitrogen. A photomicrograph of the fracture surface of one–half of the specimen is shown in Fig. 28; the crack front is relatively straight. The average crack extension for the transgranular region and the total crack advance were determined by taking ≈20 measurements across the width of the specimen. The measured total crack extension was greater than the value determined from the DC potential measurements, most likely because of several unbroken ligaments in the intergranular region. Thus, using the common assumption that ligaments have little
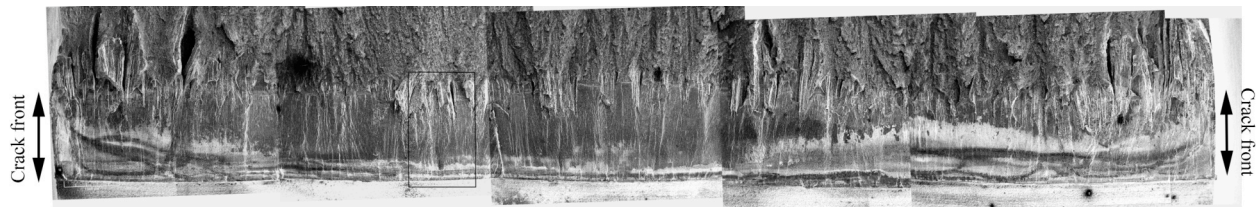

Figure 28. Photomicrograph of the fracture surface of specimen CT31-W01 TS.
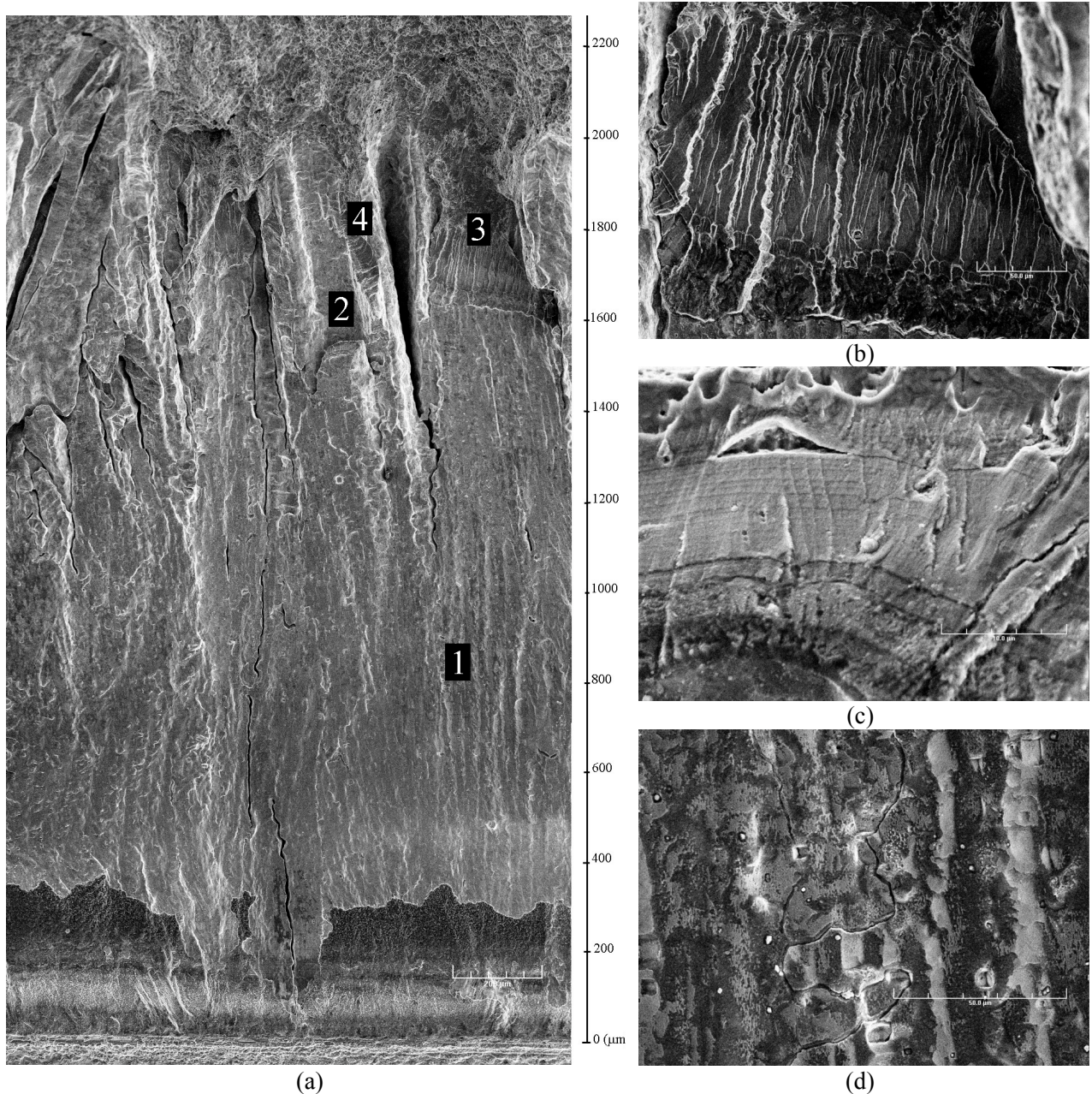
Figure 29.   A high magnification micrograph showing entire crack extension in the center of specimen CT31–W01 TS. Micrographs b, c, and d are from locations 3, 2, and 1 in micrograph.

tendency to develop during cyclic loading the transgranular data was not corrected, and a factor 2.1 was applied to the DC potential data for the intergranular region; the corrected data are given in Table 5.

To correlate different fracture modes with the test parameters (Table 5), the fracture surface of the specimen was also investigated by high magnification SEM. Figure 29 is a collage of micrographs showing the entire crack extension in a region corresponding to the boxed area of Fig. 28.   High magnification micrograph of locations designated 3, 2, and 1 in Fig. 29a are shown in Figs. 29b, c, and d, respectively.

The results indicate that cracking initiated and progressed in a transgranular (TG) mode along the columnar grains and through the dendritic microstructure up to approximately 1300-1400 μm. At longer crack extensions, the fracture mode is predominantly intergranular (IG) with significant secondary IG cracks parallel to the direction of crack advance (Fig. 29a). Table 5 indicates that the change to an IG fracture mode occurred during test period 5 when the rise time was increased from 10 to 100 s. Nevertheless, secondary IG cracks apparently are observed quite early during the test (Figs. 29a and d), but, as shown later in this section, evidence suggests that the secondary IG cracking most likely occurred during the high rise–time testing and extended back into the already cracked region. Figure 29c (location "2" in Fig. 29a) is a high magnification micrograph from the area corresponding to the high rise time testing, and shows the highly deformed facet of an IG crack. Further, close to the end of the crack front, Fig. 29b (location "3" in Fig. 29a) shows a TG stepped fracture surface.

The transition from TG to IG fracture is shown in Fig. 30a. The top–center brighter area of the figure shows IG cracks with the dendrites oriented perpendicular to the direction of crack advance, whereas the adjacent grain with the dendrites oriented parallel to the direction of crack advance shows TG fracture. The existing CGR data for Ni-alloy welds indicate that in PWR environments, the growth rates parallel to the columnar grain structure (TS orientation) are generally a factor of two greater than those perpendicular to the columnar grain structure (TL orientation). This conclusion may not be true in all cases. The onset of IG cracking seems to have occurred sooner for the perpendicular grains.

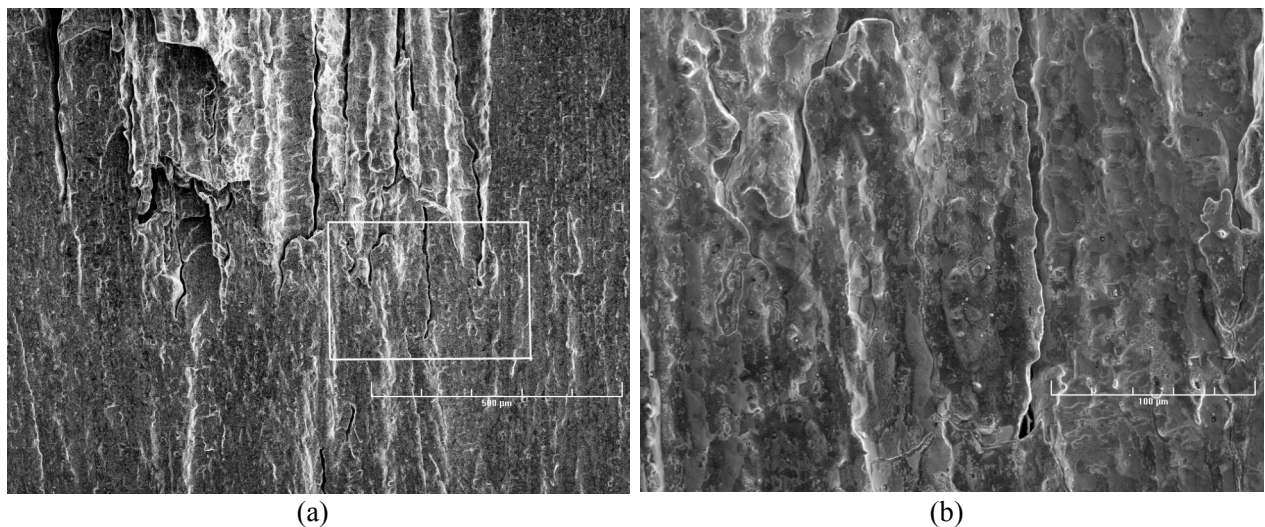(a)   (b)

Figure 30. (a) Transition from TG to IG fracture and (b) higher magnification micrograph of the boxed area showing the tip of a few secondary cracks. Crack extension from bottom to top of the figure.

Another significant observation concerns the apparent formation of secondary IG cracks quite early during the test. A few examples are shown in the boxed area of Fig. 30a, and at higher magnification in Fig. 30b. The cracks seem to blunt in the TG region, suggesting that they had actually originated in the IG region and propagated back into the TG region. This behavior is substantiated further by additional micrographs in Fig. 31.

Figure 31a identifies an area in the TG region where IG cracks were observed (boxed area). A high magnification micrograph of the region is shown in Fig. 31b, where the two most prominent cracks are designated "1" and "2". The two cracks appear to shrink as they advance in the TG region; furthermore, the tips appear blunt, as shown in Figs. 31c and d. Such observations lend further support to the
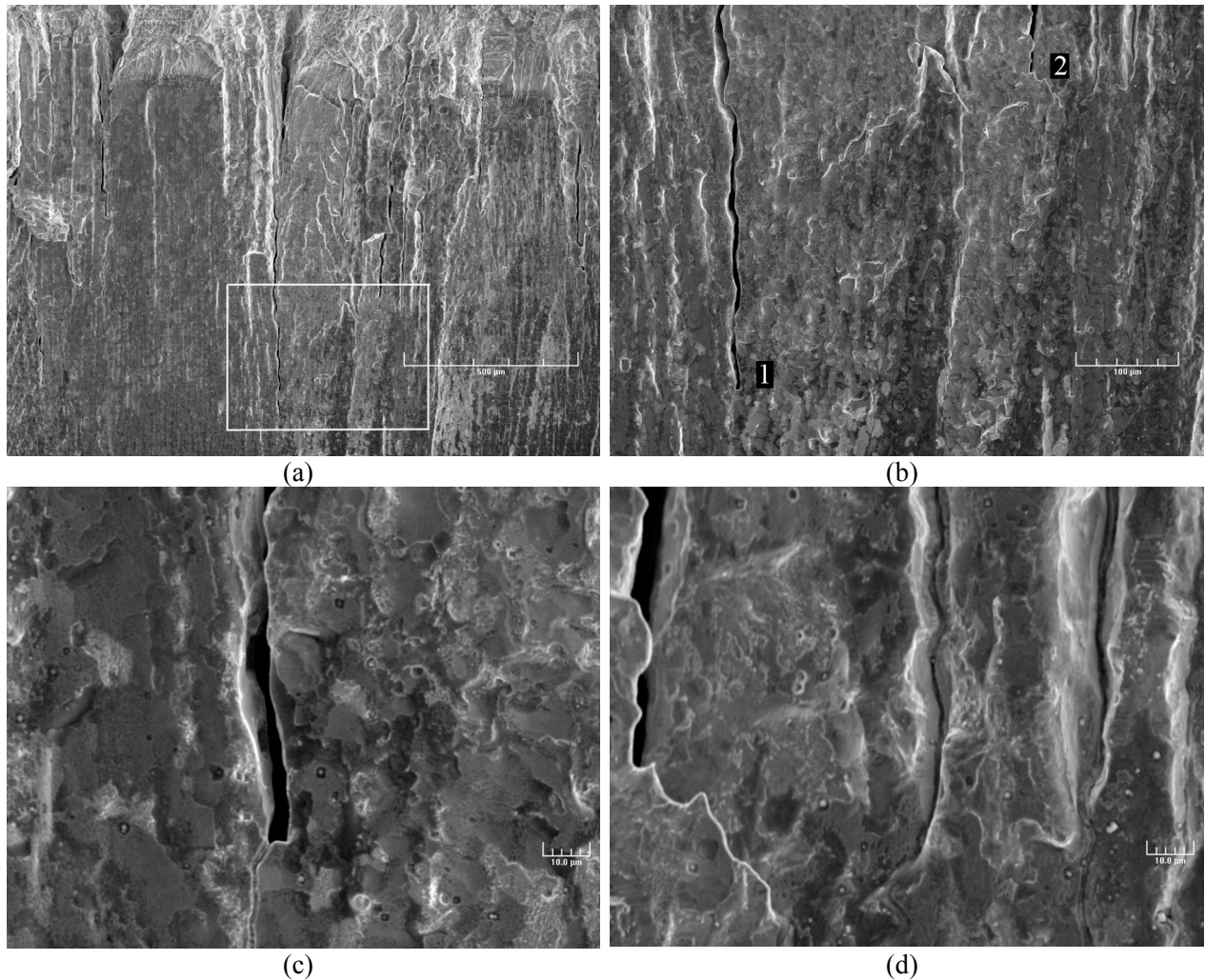
Figure 31. (a) Mixed TG and IG fracture modes, (b) high magnification micrograph of the boxed area, and (c, d) micrographs showing the crack tips at locations "1" and "2" in micrograph b. Crack extension from bottom to top of the figure.

hypothesis that the secondary IG cracks most likely originated in the IG region and propagated opposite to the direction of crack advance into the TG region.

The next two sets of micrographs focus on the region obtained near the end of the test during periods with a hold time and/or a high rise time. As mentioned earlier the crack extension measured after the test was ≈35% greater than that determined by the DC potential measurements. The present results indicate that the crack front might have advanced in a nonuniform manner, faster along some grain orientations, leaving behind more–resistant, unbroken ligaments. In turn these ligaments would cause the DC potential technique to underestimate the crack length. The first set of micrographs, Figs. 32a and c, show two examples where ductile fracture is adjacent to IG cracking.   The high magnification micrographs (Figs. 32b, d) were obtained at the positions indicated by arrows in Figs. 32a and c. It thus appears very likely that some IG crack fronts propagated independently of each other, and the unbroken ligament ruptured when the specimen was fractured in air.

By contrast, the second set of micrographs, Fig. 33, documents cases of various TG fracture morphologies observed in the last test region. These micrographs show stepped TG (Figs. 33a, b) and quasi-cleavage with cleavage steps and crack arrest markings (Figs. 33c, d). These cases of TG in a test condition favoring IG are probably similar to those described in Fig. 32, i.e., grains of unfavorable orientation for crack advance situated between two faster propagating regions. It can thus be envisaged that high local stresses combined with the effect of environment caused these grains to crack in a TG mode.

In summary, the examination of the fracture surface of the CT31-W01 TS specimen revealed that the fracture mode correlates well with the testing condition. Specifically, high rise times or long hold periods favor IGSCC. Also, IG cracking apparently advanced more readily along some grain orientations than others, resulting in a crack front with occasional unbroken ligaments and few regions of TG cracking.

(a)　　　　　　　　　　　　　　　　　(b)
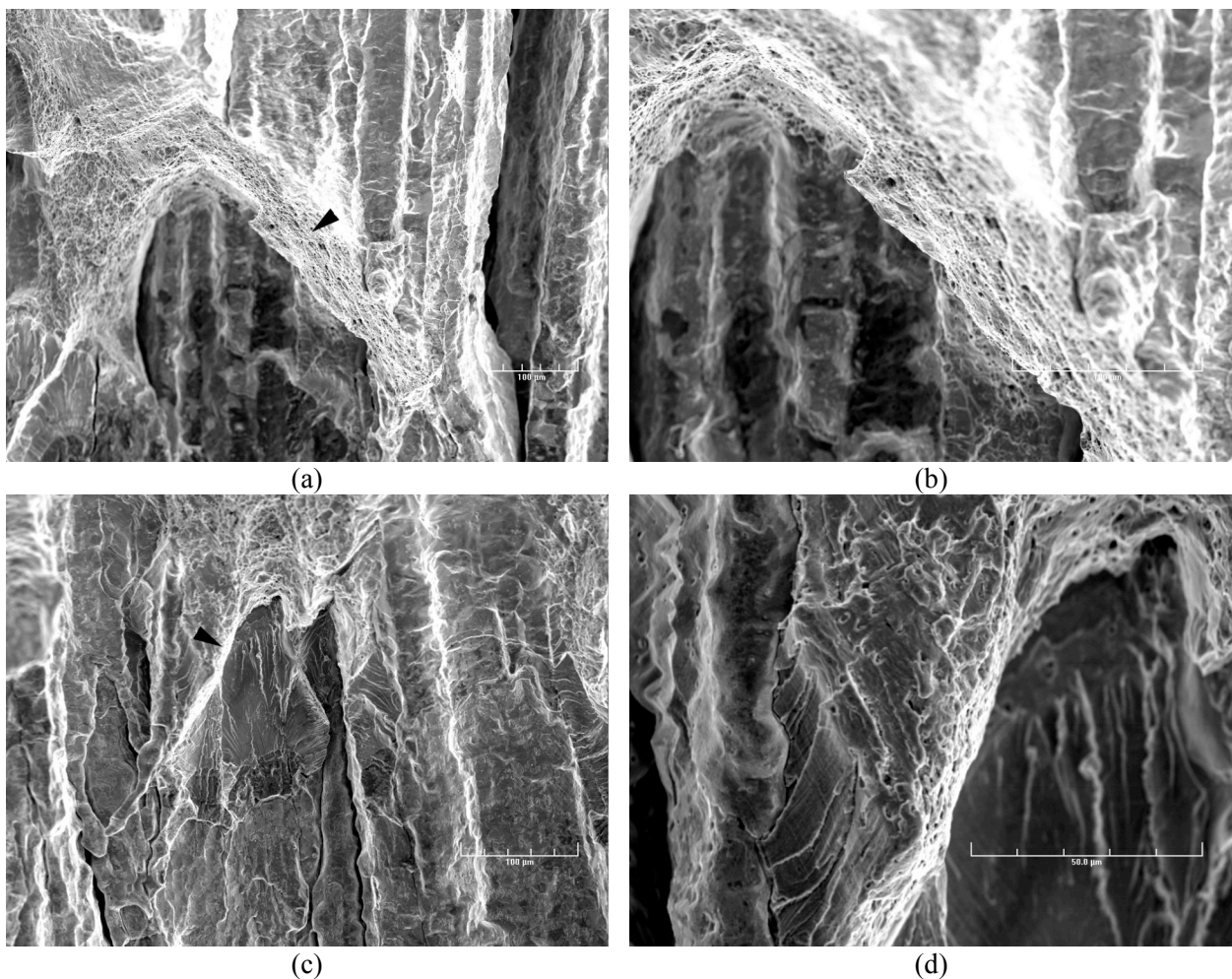
(c)　　　　　　　　　　　　　　　　　(d)

Figure 32.　(a, c) Photomicrographs detailing the fracture in a region during test periods with a hold time and/or a high rise time and (b, d) high magnification micrographs of positions indicated by arrows. Crack extension from bottom to top of the figure.
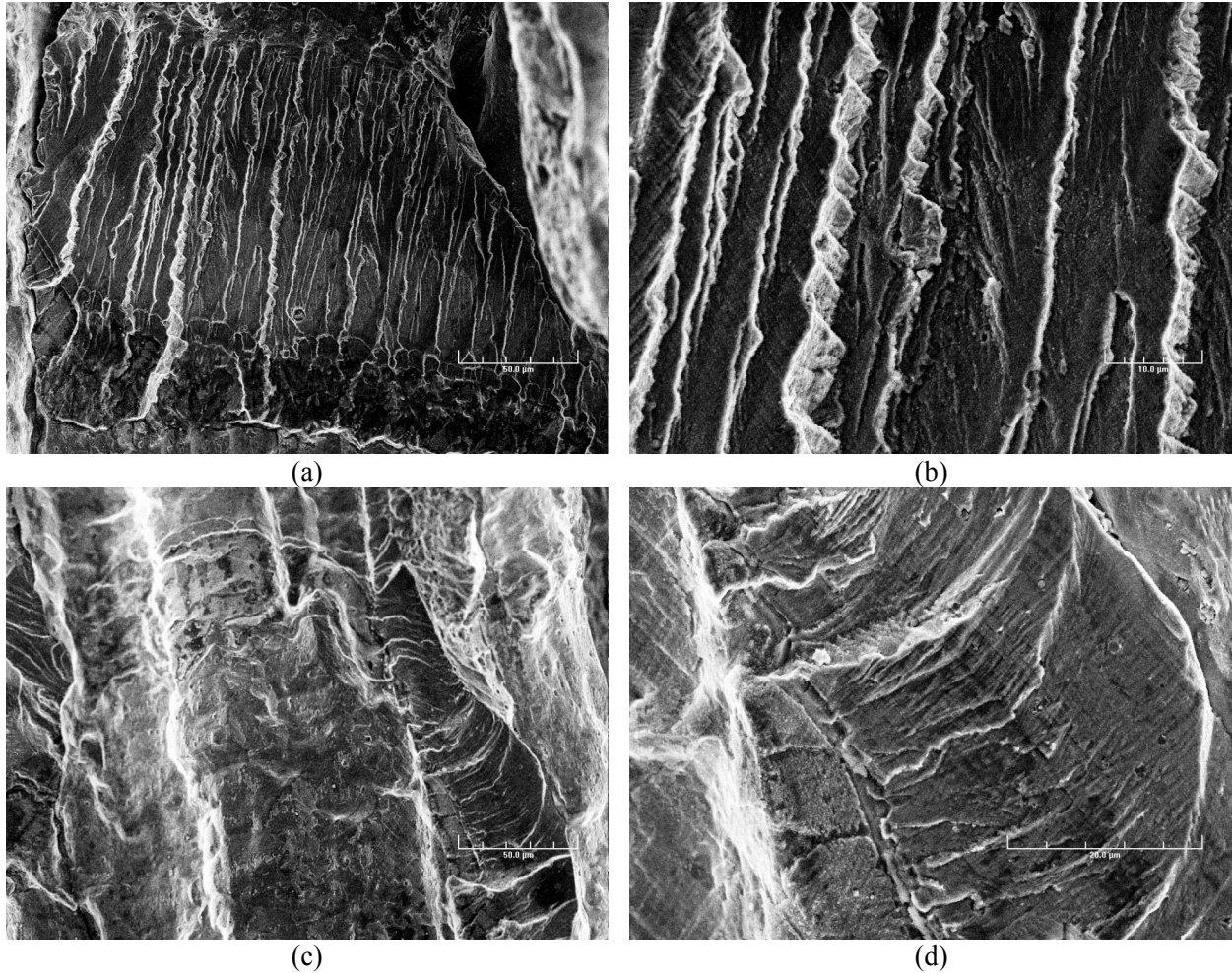
Figure 33. (a, c) Photomicrographs detailing the fracture in a region during test periods with a hold time and/or a high rise time, and (b, d) high magnification micrographs.

### 4.1.2   Crack Growth Data for Double-J Weld Specimen CT31-W02 TS

A second CGR test was conducted on a double–J weld specimen in the PWR environment at 320°C to verify the earlier results. The test was started with the water system operating in the once–through mode at a flow rate of ≈10 cc/min. The system was operated for about a week for the environmental conditions to stabilize. The specimen was fatigue precracked at R = 0.3, initial K_{max} = 23 MPa m$^{1/2}$, triangular waveform, and 0.5 Hz frequency. Under these conditions, crack growth was relatively fast, the crack extended by ≈12.5 mm in ≈14 h, and K_{max} increased from ≈23 to 43 MPa m$^{0.5}$, which is higher than intended. To emerge from the plastic zone associated with the high K_{max}, the specimen was cycled at a K_{max} of ≈29 MPa m$^{0.5}$ using a saw–tooth waveform with a 12–s rise time. The sample was then set at constant load and K_{max} of 30.5–49.5 MPa m$^{1/2}$. The experimental conditions and results for the test are given in Table 6; the changes in crack length and K_{max} with time are shown in Fig. 34.

34

Table 6. Crack growth data for specimen CT31-W02 TS of Alloy 182 SMA weld in PWR water[a] at 320°C.

Test Period	Test Time, h	ECP[b] (SHE) mV	O_2 Conc.,[b] ppb	Load Ratio R	Rise Time, s	Down Time, s	Hold Time, s	K_{max}, MPa·m$^{1/2}$	ΔK, MPa·m$^{1/2}$	CGR_{env}, m/s	Estimated CGR_{air}, m/s	Crack Length, mm
Pre a	129	−679	<10	0.3	1	1	0	23.7	16.6	1.83E−07	3.37E−08	13.928
Pre b	132	−679	<10	0.3	1	1	0	26.4	18.5	3.10E−07	2.62E−08	16.026
Pre c	136	−679	<10	0.3	1	1	0	29.7	20.8	4.55E−07	4.24E−08	18.356
Pre d	138	−679	<10	0.3	1	1	0	34.9	24.4	6.10E−07	8.24E−08	21.470
Pre e	141	−679	<10	0.3	1	1	0	43.3	30.3	7.48E−07	1.99E−07	25.274
1	339	−681	<10	0.5	12	2	0	28.8	14.4	2.08E−09	1.36E−09	25.872
2	359	−672	<10	0.5	12	2	0	29.9	15.0	6.91E−09	1.58E−09	26.417
3	599	–	<10	1.0	–	–	–	30.5	–	4.22E−10	–	26.708
4	812	–	<10	1.0	–	–	–	36.4	–	3.94E−10	–	27.097
5	1157	–	<10	1.0	–	–	–	49.5	–	7.29E−10	–	28.185

[a]Simulated PWR water with 2 ppm Li, 1100 ppm B, and 2 ppm dissolved hydrogen ($\approx$23 cc/kg).
[b]Represents values in the effluent; ECP values are for Alloy 600 electrode, conductivity was $\approx$22 µS/cm in the effluent.
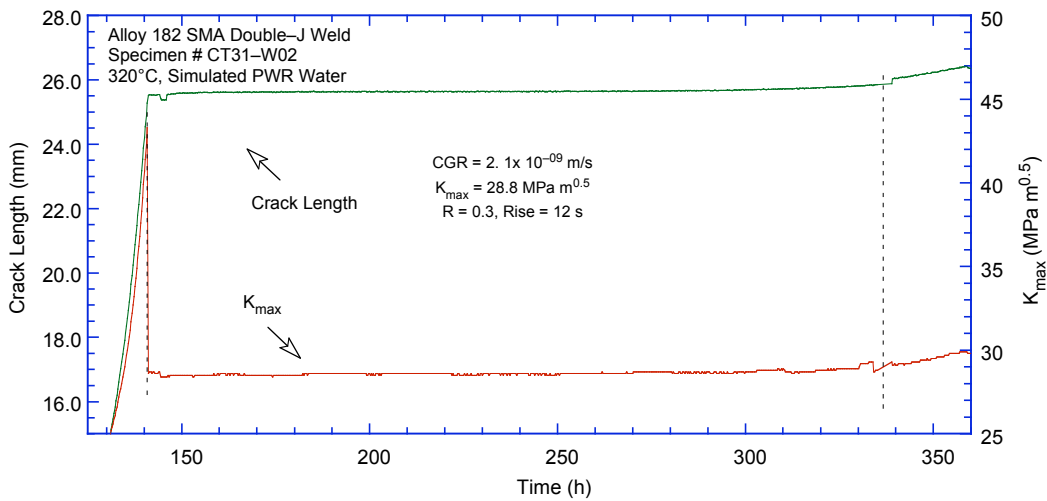
(a)
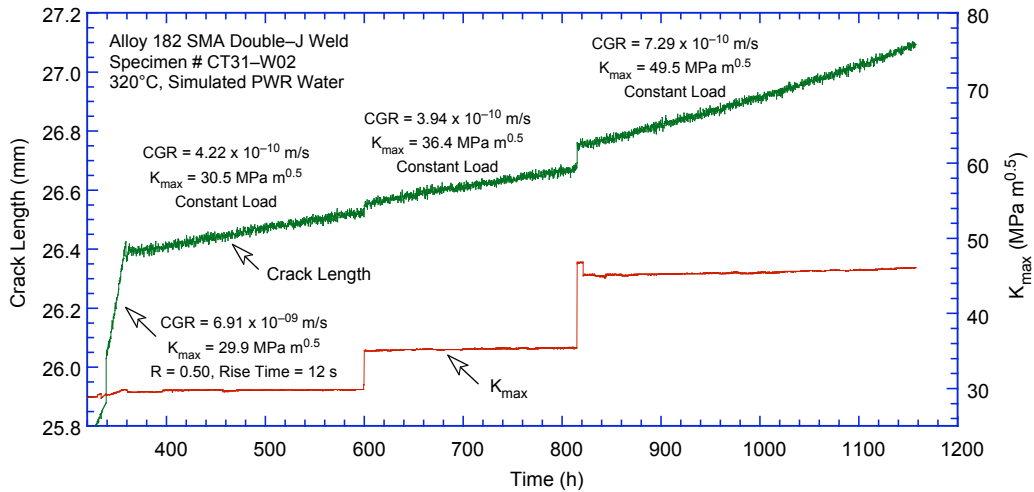
(b)

Figure 34. Crack length vs. time for Alloy 182 SMA double–J weld specimen CT31-W02 TS in simulated PWR environment at 320°C during test periods (a) 1–3 and (b) 4–5.

35

Figure 35 shows the fracture surface of specimen CT31-W02 TS (approximately 1/4 of the width was cut off prior to breaking the sample apart, to enable the examination of the cross section). The fracture surface was exclusively TG until the constant load testing, at which point the fracture mode switched to IG. The IG fracture area is bound by the green and red lines in Fig. 35. The red line also shows the final crack front. The testing procedure resulted in a relatively straight crack front.
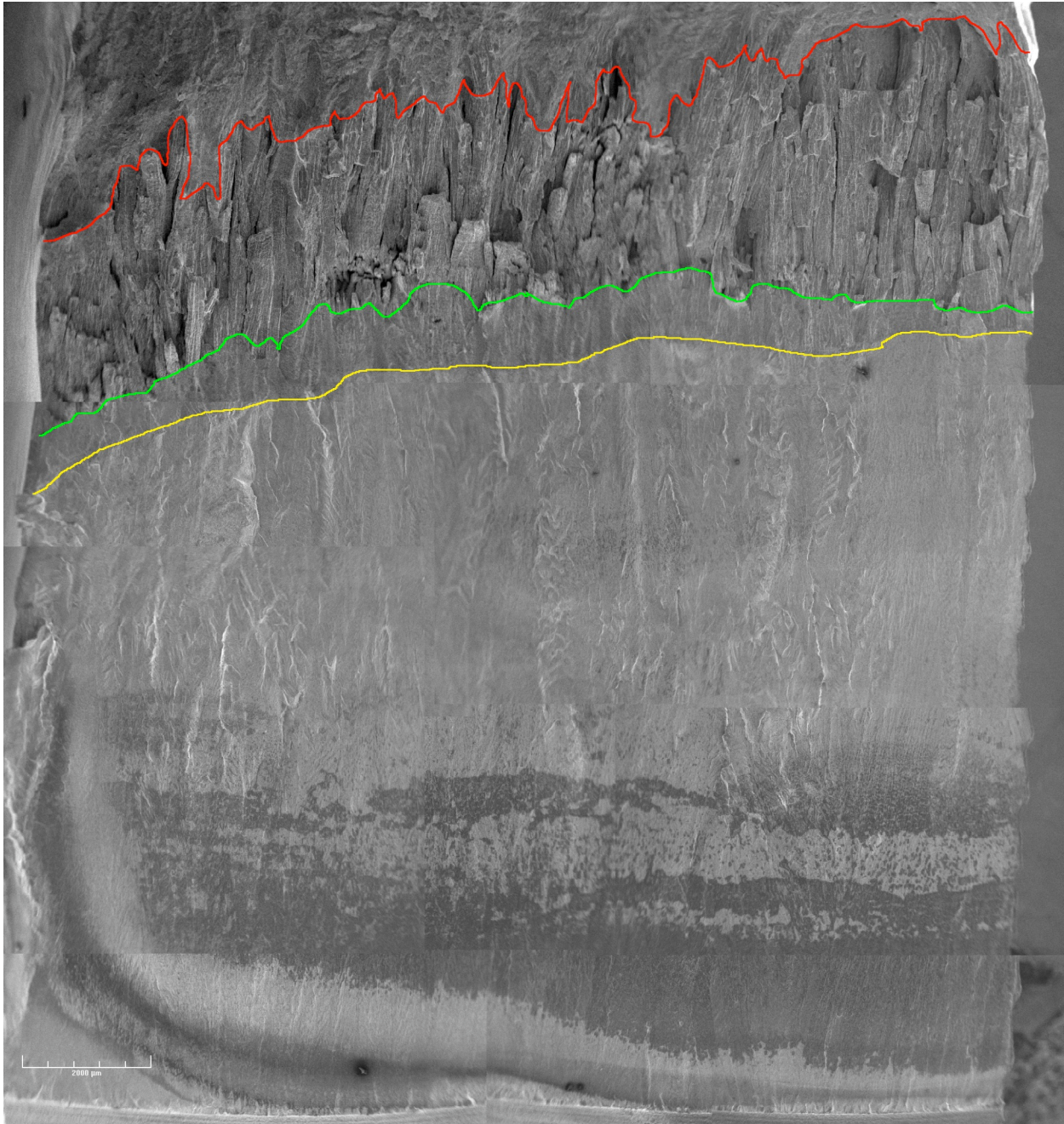

Figure 35.   Fracture surface of specimen CT31-W02 TS. Crack extension from bottom to top of the figure.

Figure 36 shows the cross section of CT31-W02 TS. Near the end of the test (boxed area in Fig. 36 a) the crack line becomes discontinuous. This condition, along with possible cases where the two surfaces of the crack touch each other, partially causes the DC potential measurements to underestimate

the full extent of the crack. However, unlike the previous example, the precrack region in this case is TG; thus it is expected to be measured accurately by the DC potential method. For this test, only CGR data resulting from the IG periods were corrected. As such, based on Fig. 35 the IG region was measured to be 3.31 mm, a factor of 2.6 larger than the value obtained from DC potential measurements (the data in Table 6 have been corrected to be consistent with the fractographic results).
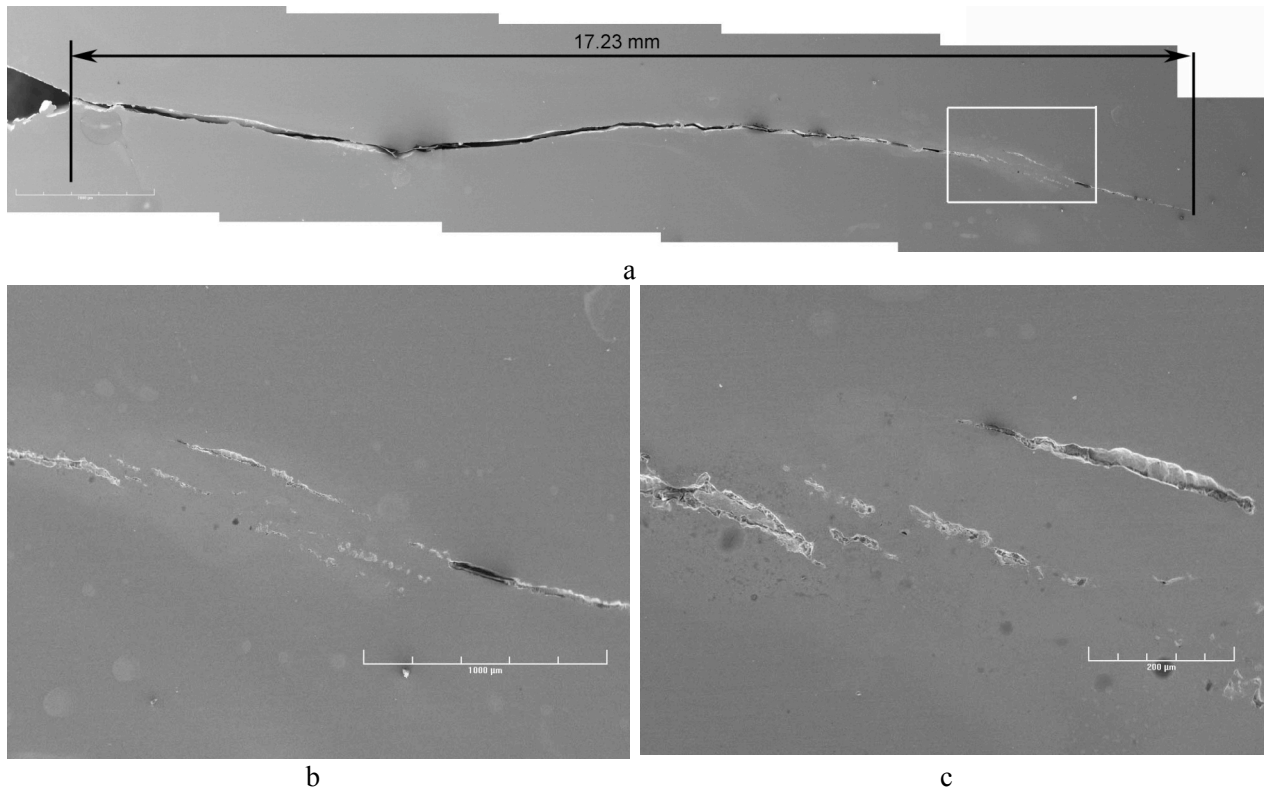

Figure 36. Micrographs showing the cross section of CT31-W02 TS.

### 4.1.3 Crack Growth Data for Deep-Groove Weld Specimen CT933-TS

This test was started in PWR water at 320°C with the system operating in once–through mode at a flow rate of ≈10 cc/min. The system was operated for about a week for the environmental conditions to stabilize. The specimen was fatigue precracked at R = 0.3, K_{max} = 23 MPa m$^{1/2}$, triangular waveform, and 0.5–Hz frequency. After ≈1–mm extension, R was increased incrementally to 0.7, and the waveform changed to sawtooth with 300–s rise time with or without a 3600–h hold period to transition to IG cracking. Finally, the test was conducted at constant load (K_{max} ≈ 30 MPa m$^{1/2}$). The specimen was next subjected to a constant load but higher K_{max} (≈34 MPa m$^{1/2}$); the applied K_{max} was increased by fatigue cycling at R = 0.5 and rise time of 30 or 300 s to increase the crack length from ≈14 to 16 mm. The experimental conditions and results for the test are given in Table 7; the changes in crack length and K_{max} with time are shown in Fig. 37.

37

Table 7.   Crack growth data for specimen CT933-TS of Alloy 182 SMA weld in PWR water[a] at 320°C.

Test Period	Test Time, h	Conduc- tivity,[b] µS/cm	DO,[b] ppb	R Load Ratio	Rise Time, s	Down Time, s	Hold Time, s	K_{max}, MPa·m$^{1/2}$	ΔK, MPa·m$^{1/2}$	CGR, m/s	CGR in Air, m/s	Crack Length, mm
Pre a	30	25.0	<10	0.3	1	1	0	23.18	16.23	2.07E-09	1.54E-08	12.609
Pre b	40	25.0	<10	0.3	10	10	0	23.32	16.32	5.80E-09	1.58E-09	12.708
1a	70	25.0	<10	0.3	10	10	0	23.87	16.71	1.05E-08	1.74E-09	13.148
1b	90	25.3	<10	0.3	10	10	0	24.57	17.20	1.47E-08	1.96E-09	13.686
2	142	25.3	<10	0.6	10	10	0	25.29	10.11	1.88E-09	5.29E-10	13.889
3	243	25.3	<10	0.7	10	10	0	25.89	7.77	6.97E-10	2.64E-10	14.027
4	506		<10	0.7	100	100	0	25.71	7.71	2.43E-10	2.57E-11	14.234
5	704		<10	0.7	300	12	0	28.46	8.54	1.18E-10	1.30E-11	14.313
6	964		<10	0.7	300	12	3600	28.60	8.58	1.15E-10	1.32E-11	14.428
7	1132		<10	1.0	–	–	–	28.72	0.00	1.05E-10	–	14.491
8	1373		<10	0.5	30	4	0	32.61	16.30	2.66E-09	8.99E-10	16.568
9	1467		<10	0.5	300	4	0	33.34	16.67	1.37E-09	9.85E-11	16.990
10			<10	1.0	–	–	–	36.88	0.00	2.53E-10	–	17.753

[a]Simulated PWR water with 2 ppm Li, 1100 ppm B, and 2 ppm dissolved hydrogen (≈23 cc/kg).
[b]Represents values in the effluent; ECP was measured at 289°C.
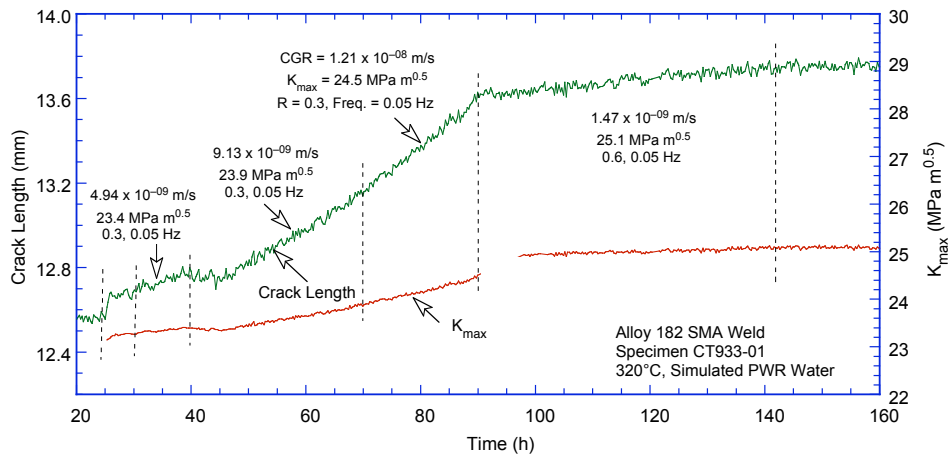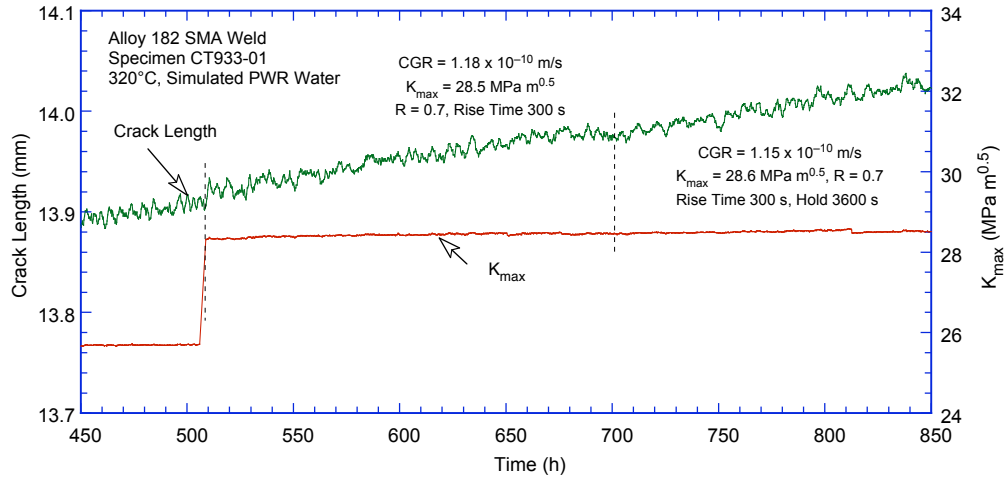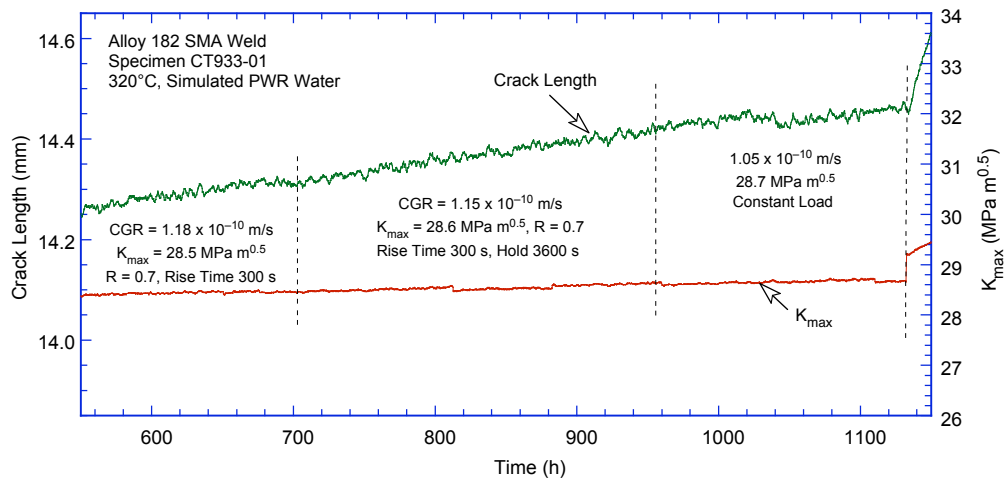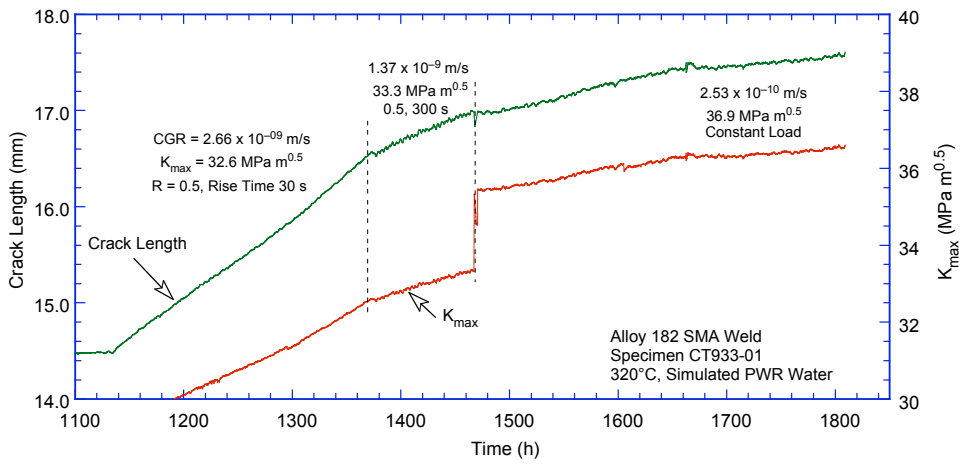

(a)
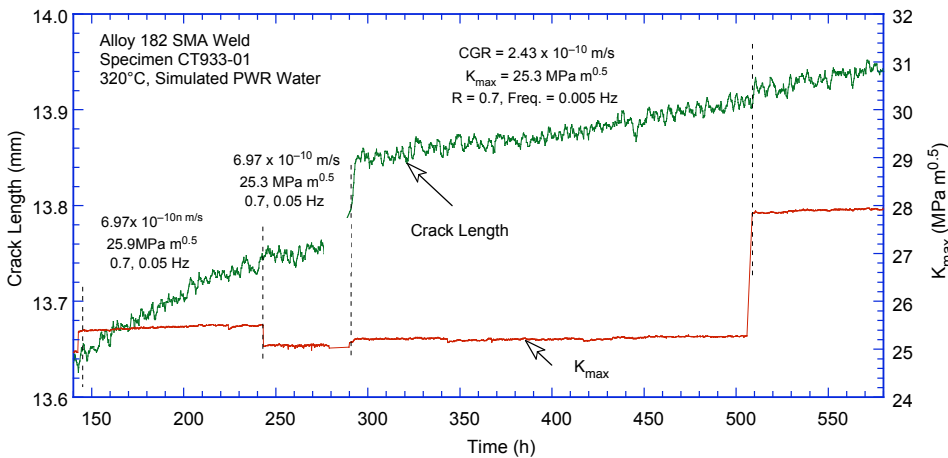
(b)

Figure 37.   Crack length vs. time for laboratory–prepared Alloy 182 weld specimen CT933–TS in simulated PWR water at 320°C during periods (a) precracking–period 2, (b) 3–4, (c) 5–6, (d) 7–8, and (e) 9–10.

(c)

(d)

(e)

Figure 37.   (Contd.)

The fractured compact tension specimen CT933-TS was examined by SEM in cross section and on the fracture surface. Figure 38 shows the entire crack length on the cross–section sample. Based on this cross section, the crack length was estimated at approximately 5.05 mm. Also, for this section (close to one side of the sample), the onset of intergranular (IG) fracture was estimated at 2.28 mm.
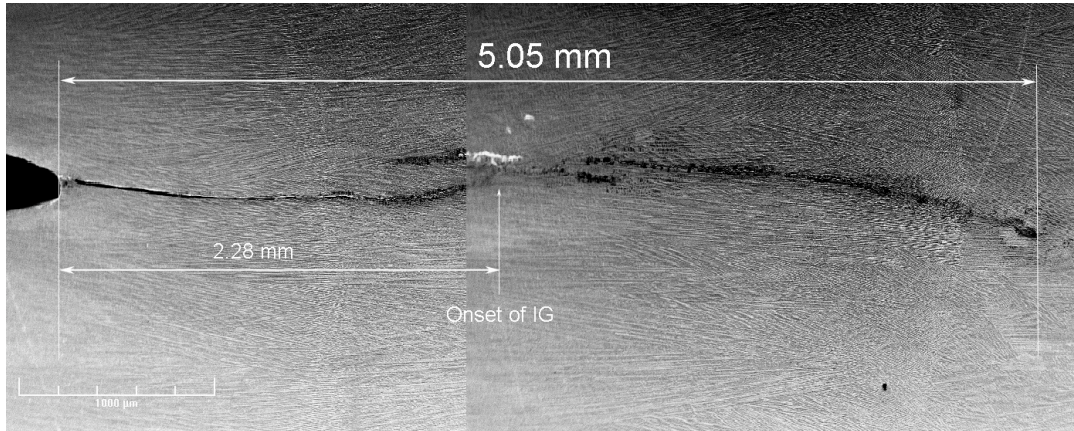

5.05 mm

2.28 mm

Onset of IG

Figure 38. Crack front in cross section of sample CT933-TS.

Figure 39 shows the entire fracture surface of this specimen. Following pre-cracking, the fracture turned into a mainly trangranular (TG) mode, the exception being the center of the sample where the fracture mode is primarily intergranular (IG). Nevertheless, we observe that the testing procedure resulted in a relatively straight crack front. The average crack extension for the transgranular region and the total crack advance were determined by taking ≈20 measurements across the width of the specimen. The measured total crack extension was greater than the value determined from the DC potential measurements. The DC potential data was scaled proportionally: a factor 1.24 was applied to the transgranular data and a factor 1.65 was applied to the DC potential data for the intergranular region; the corrected data are given in Table 7.
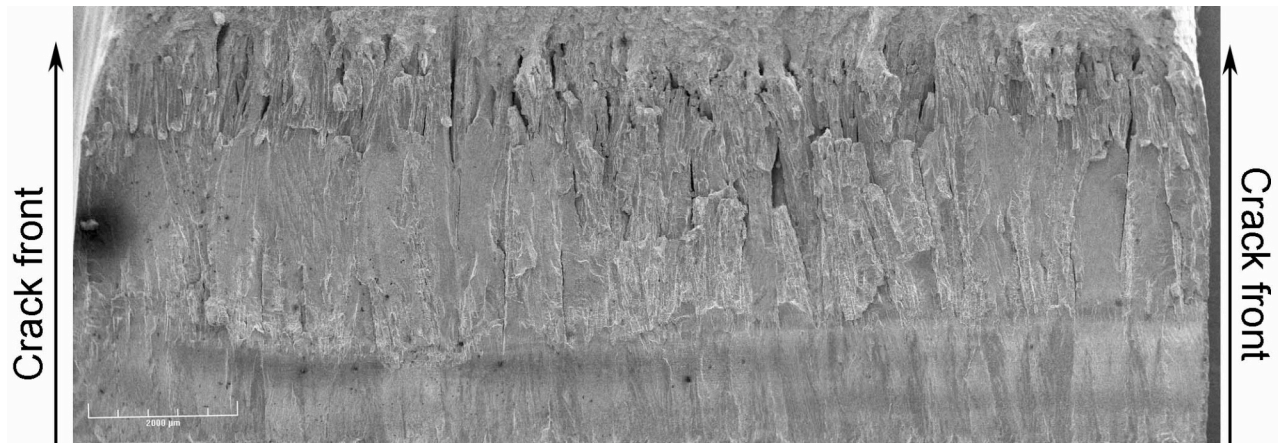

Crack front

Crack front

Figure 39. Crack front on fracture surface of sample CT933-TS.

An additional collage from the sample surface was constructed with the purpose of illustrating the fracture modes (Fig. 40). The set of pictures shown in Fig. 40a was taken in the middle of the sample, where the IG cracking mode occurred earlier than close to the sides. Figure 40b shows the co-existence of TG and IG cracking modes in the early stages of the experiment (position 1). Figure 40c illustrates IG

cracking, typical for the weld microstructure (position 2). Figure 40d shows ductile fracture in the middle of the IG fracture mode (position 3), which was most likely due to an unbroken ligament.
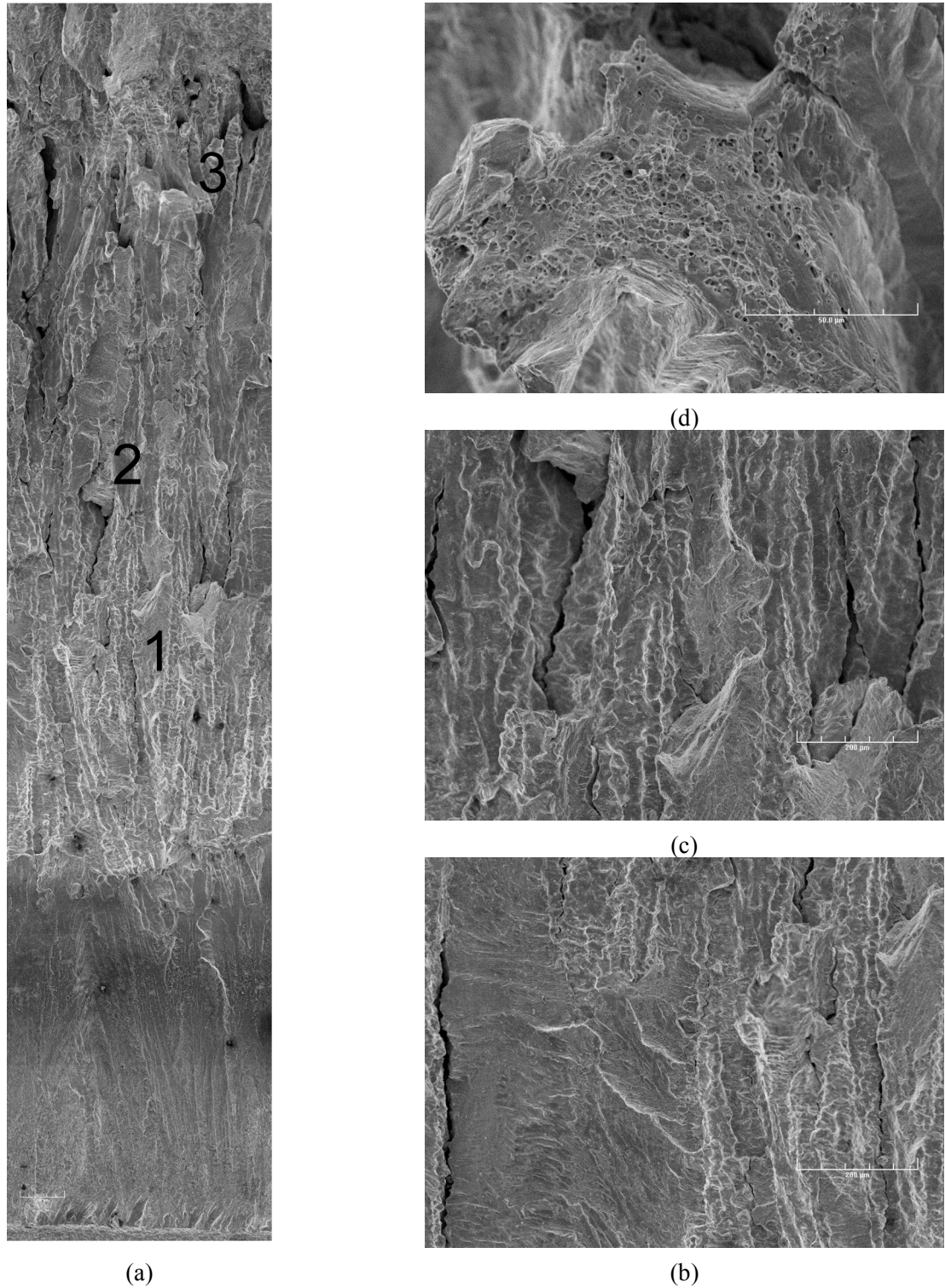

Figure 40. (a) Crack front on sample CT933-TS, where several fracture modes are identified: (b) transition from TG to IG; (c) IG; and (d) ductile rupture in the IG region. Crack extension is from bottom to top of the figure.

### 4.1.4 Crack Growth Data for Deep-Groove Weld Specimen CT933-TL

The experimental conditions and results for testing of CT933–TL are shown in Table 8, and the changes in crack length and K_{max} with time are shown in Fig. 41. The specimen was fatigue precracked with a triangular waveform at $R = 0.5$ and $K_{max} = 21$ MPa m$^{1/2}$, followed by cycling with a trapezoidal waveform at $R = 0.5$ and $K_{max} = 21.6$ MPa m$^{1/2}$. The specimen was then set at constant load at $K_{max} = 21.6$ MPa m$^{1/2}$ for $\approx$200 h. The specimen was next cycled at $R = 0.5$, at increasing rise times, and set at constant load at $K_{max} = 21.8$ and 30.9 MPa m$^{1/2}$. The specimen was next cycled with the goal of reaching $K_{max} = 35$ MPa m$^{1/2}$, and set at constant load. Finally, the sample was again cycled to reach approximately $K_{max} = 49.2$ MPa m$^{1/2}$, and set at constant load. The effluent water conductivity was monitored continuously, while the effluent DO and ECPs of a Pt electrode and Alloy 600 electrode downstream from the autoclave were measured periodically. The water flow rate was $\approx$25 cc/min. The ECPs of Pt and Alloy 600 electrodes were –690 and –693 mV (SHE), respectively.

Table 8. Crack growth data for specimen CT933-TL of Alloy 182 SMA weld in PWR water[a] at 320°C.

Test Period	Test Time, h	Cond.,[b] µS/cm	O_2 Conc.,[b] ppb	Load Ratio R	Rise Time, s	Down Time, s	Hold Time, s	K_{max}, MPa·m$^{1/2}$	ΔK, MPa·m$^{1/2}$	CGR_{env}, m/s	Estimated CGR_{air}, m/s	Crack Length, mm
Pre a	73	22	<10	0.3	0.5	0.5	0	21.2	14.8	1.12E-08	1.07E-08	12.791
Pre b	96	22	<10	0.3	0.5	0.5	0	21.4	15.0	1.25E-08	2.22E-08	12.945
1	191	22	<10	0.5	300	12	0	21.6	10.8	3.61E-10	1.65E-11	13.110
2	385	22	<10	1	–	–	0	21.63	0.00	2.68E-12	–	13.153
3	500	22	<10	0.5	300	12	0	21.67	10.83	1.08E-10	1.68E-11	13.164
4	598	22	<10	0.5	1000	12	0	21.70	10.85	4.03E-11	5.07E-12	13.181
5	860	22	<10	1	–	–	0	21.81	0.00	4.46E-11	–	13.259
6a	867.0	22	<10	0.3	1	1	0	23.52	16.46	6.82E-09	1.63E-08	13.309
6b	890.0	22	<10	0.3	1	1	0	23.72	16.61	1.09E-08	1.69E-08	13.470
6c	913.0	22	<10	0.3	1	1	0	23.59	16.51	1.62E-08	1.66E-08	13.669
6d	935.0	22	<10	0.3	1	1	0	24.15	16.90	1.33E-08	3.64E-08	13.822
7	1,002.0	22	<10	0.5	12	2	0	24.42	12.21	7.14E-10	6.86E-10	14.208
8	1,026.0	22	<10	0.5	12	2	0	26.50	13.25	1.40E-09	9.60E-10	14.321
9	1,073.0	22	<10	0.5	1	1	0	28.66	14.33	1.83E-08	1.59E-08	15.823
10	1,102.0	22	<10	0.5	300	12	0	30.63	15.31	1.05E-09	6.95E-11	15.957
11	1,368.0	22	<10	1	–	–	0	31.01	0.00	9.04E-11	–	16.046
12a	1,374.0	22	<10	0.3	1	1	0	32.23	22.56	9.04E-08	5.95E-08	16.875
12b	1,391.0	22	<10	0.3	1	1	0	32.88	23.02	7.54E-07	6.46E-08	17.324
13	1,398.0	22	<10	0.5	30	2	0	34.91	17.45	4.29E-08	1.19E-09	18.431
14	1,439.0	22	<10	0.5	1000	12	0	35.19	17.59	5.98E-11	3.68E-11	18.586
15	1,633.0	22	<10	1	–	–	0	35.43	0.00	8.10E-11	–	18.740
16	1,638.0	22	<10	0.3	1	1	0	37.36	26.16	1.98E-07	1.09E-07	19.769
17	1,651.0	22	<10	0.3	30	1	0	39.51	27.66	2.46E-08	4.57E-09	20.834
18	1,656.0	22	<10	0.3	1	1	0	46.67	32.67	3.81E-07	2.72E-07	23.860
19	1,663.0	22	<10	0.5	300	12	0	49.16	24.58	2.15E-08	4.84E-10	24.778
20	2,137.0	22	<10	1	–	–	0	50.01	0.00	1.57E-10	–	25.048
21	2,141.0	22	<10	0.5	300	12	0	51.61	25.12	2.52E-08	5.29E-10	25.593

[a]Simulated PWR water with 2 ppm Li, 1100 ppm B, and 2 ppm dissolved hydrogen ($\approx$23 cc/kg).
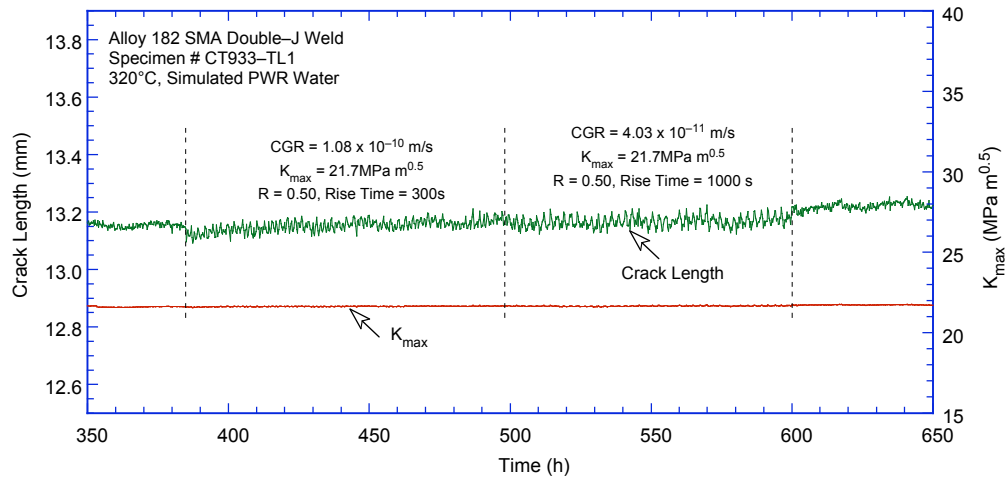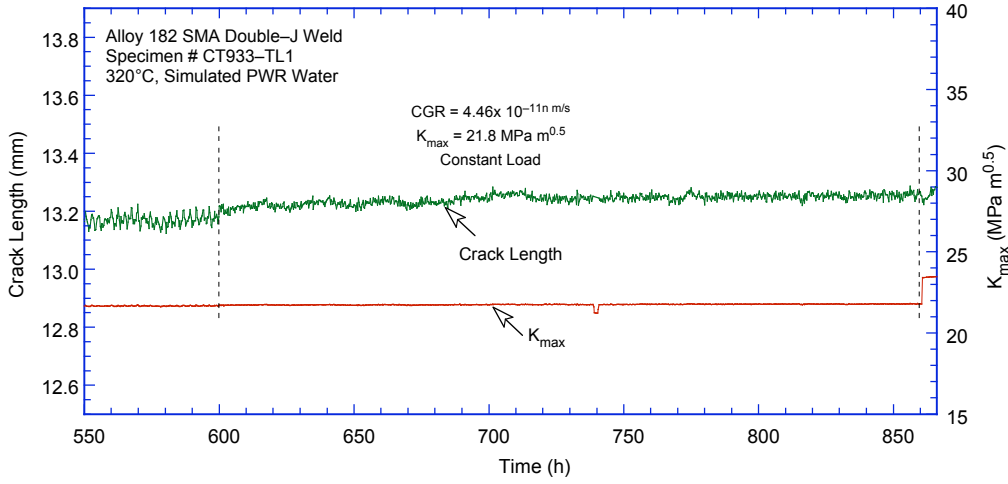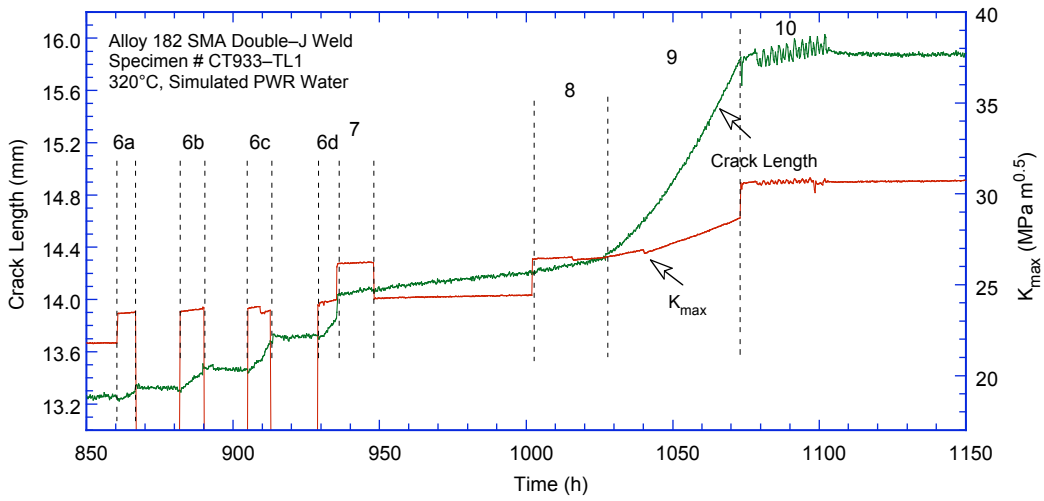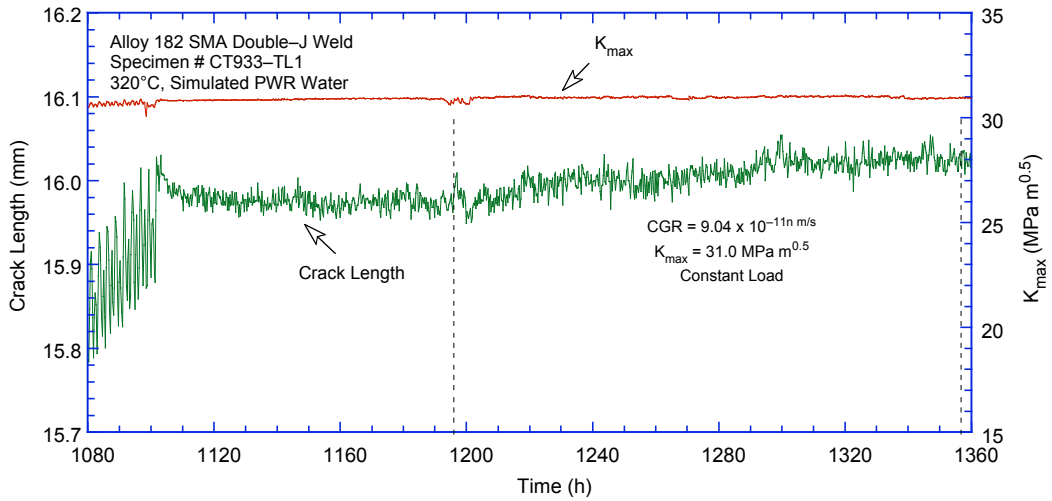[b]Represents values in the effluent.
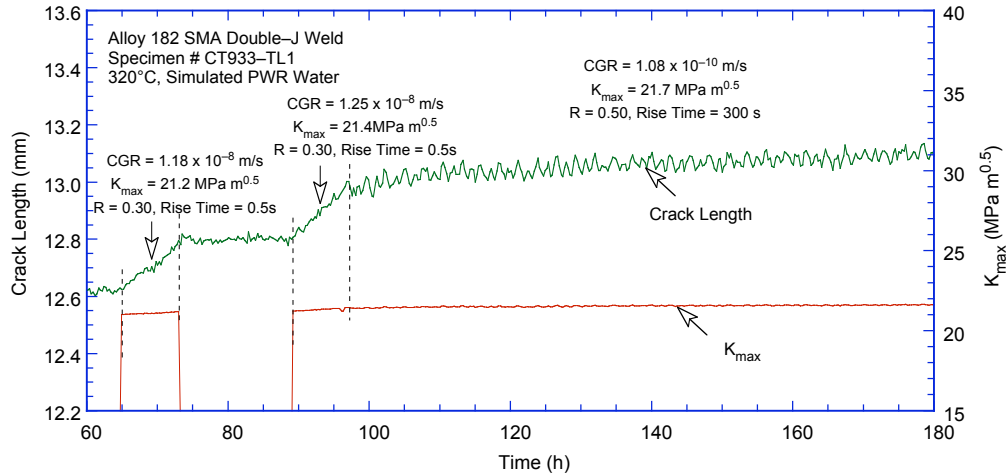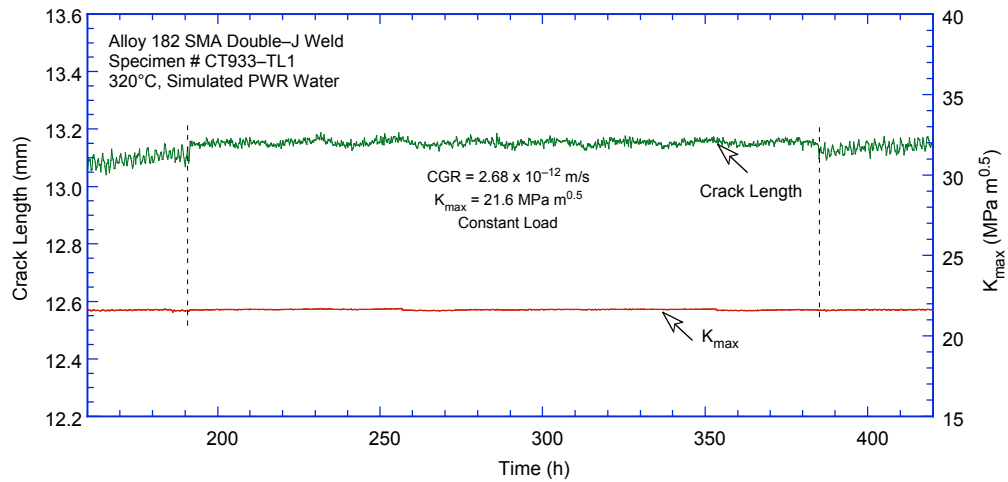
Figure 41. Crack length vs. time for Alloy 182 weld specimen CT933-TL in simulated PWR environment at 320°C during test periods (a) precracking–1, (b) 2, (c) 3–4, (d) 5, (e) 6–10, (f) 11, (g) 12-14, (h) 15, (i) 16-19, and (j) 20-21.
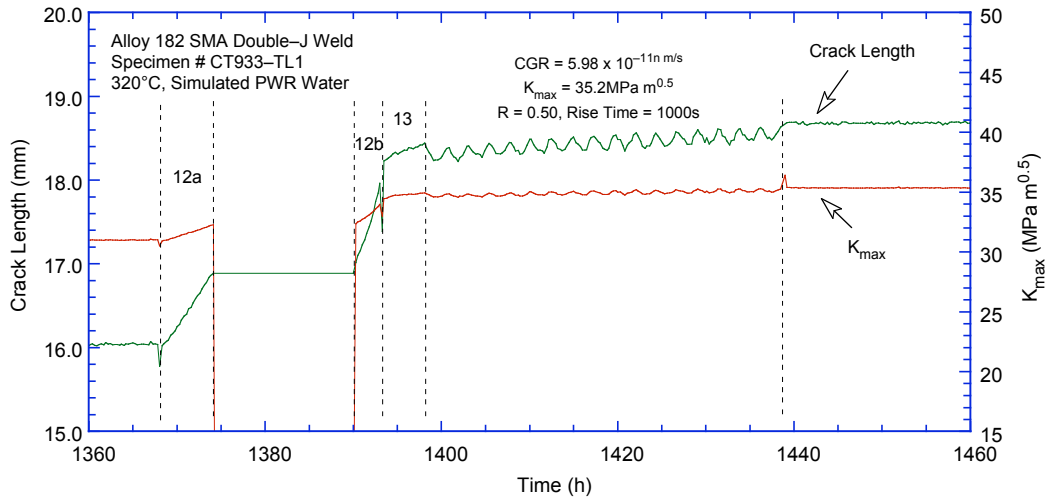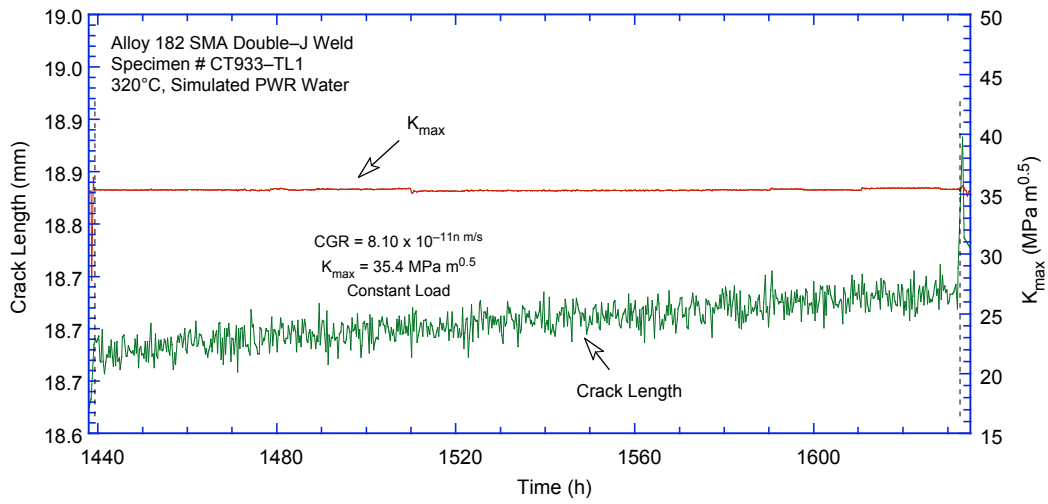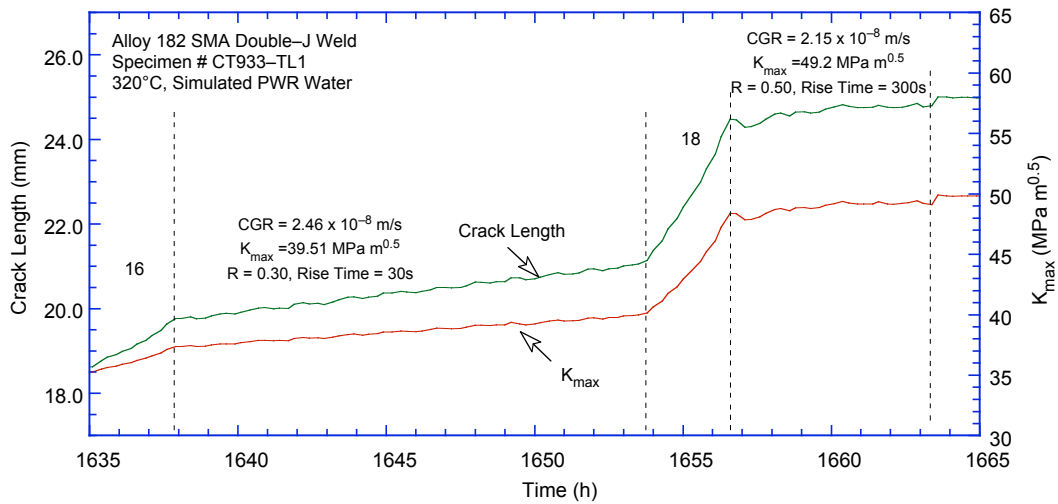
(d)

(e)

(f)

Figure 41.   (Contd.)
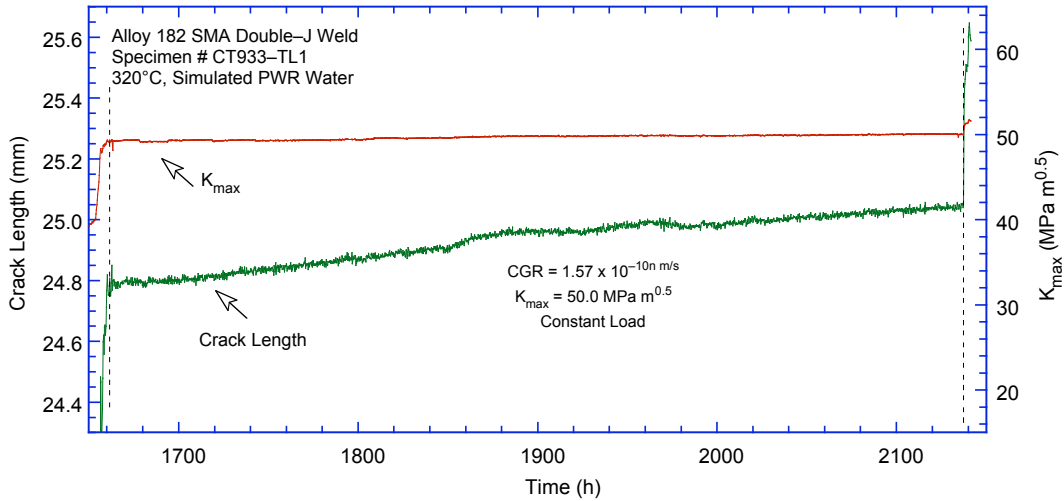
44

(g)

Alloy 182 SMA Double–J Weld
Specimen # CT933–TL1
320°C, Simulated PWR Water

CGR = 5.98×10^{-11n} m/s
K_{max} = 35.2MPa m$^{0.5}$
R = 0.50, Rise Time = 1000s

Crack Length

K_{max}

12a

12b

13

Crack Length (mm)

K_{max} (MPa m$^{0.5}$)

Time (h)

(g)

(h)

Alloy 182 SMA Double–J Weld
Specimen # CT933–TL1
320°C, Simulated PWR Water

K_{max}

CGR = 8.10×10^{-11n} m/s
K_{max} = 35.4 MPa m$^{0.5}$
Constant Load

Crack Length

Crack Length (mm)

K_{max} (MPa m$^{0.5}$)

Time (h)

(h)

(i)

Alloy 182 SMA Double–J Weld
Specimen # CT933–TL1
320°C, Simulated PWR Water

CGR = 2.15×10^{-8} m/s
K_{max} =49.2 MPa m$^{0.5}$
R = 0.50, Rise Time = 300s

18

CGR = 2.46×10^{-8} m/s
K_{max} =39.51 MPa m$^{0.5}$
R = 0.30, Rise Time = 30s

Crack Length

16

K_{max}

Crack Length (mm)

K_{max} (MPa m$^{0.5}$)

Time (h)

(i)

Figure 41.   (Contd.)

45

Alloy 182 SMA Double–J Weld
Specimen # CT933–TL1
320°C, Simulated PWR Water

K_{max}

Crack Length

CGR = 1.57 x 10^{-10n} m/s
K_{max} = 50.0 MPa m$^{0.5}$
Constant Load

Crack Length (mm)

K_{max} (MPa m$^{0.5}$)

Time (h)

(j)

Figure 41. (Contd.)

Figure 42 shows the entire fracture surface of CT933-TL, which has a relatively straight crack front. The entire crack length was measured to be 13.86 mm, slightly larger (6.2%) than the crack measurement by DC potential. This difference may be due to the fact that most of the fracture surface is transgranular, and each constant load (CL) period was followed by a cycling period, thus breaking off the ligaments that are generally believed to cause the DC potential method to underestimate the crack length.

The constant load periods CL–1 through CL–5, corresponding to the test periods 3, 5, 11, 15, and 20 (Table 8), are also indicated in Fig. 42. Examination of the fracture surface revealed that, although the fracture mode was IG during the constant load periods, the crack growth rate in this particular orientation was relatively small, causing a non-complete IG engagement during the typical 200 h of testing time in each constant load period. Nevertheless, the IG engagement was complete during CL–5 (test period 20, Table 8), which lasted approximately 500 h. Figure 43 shows the fracture surface from this last constant–load test period, and Fig. 44 shows a high magnification micrograph also from this region.
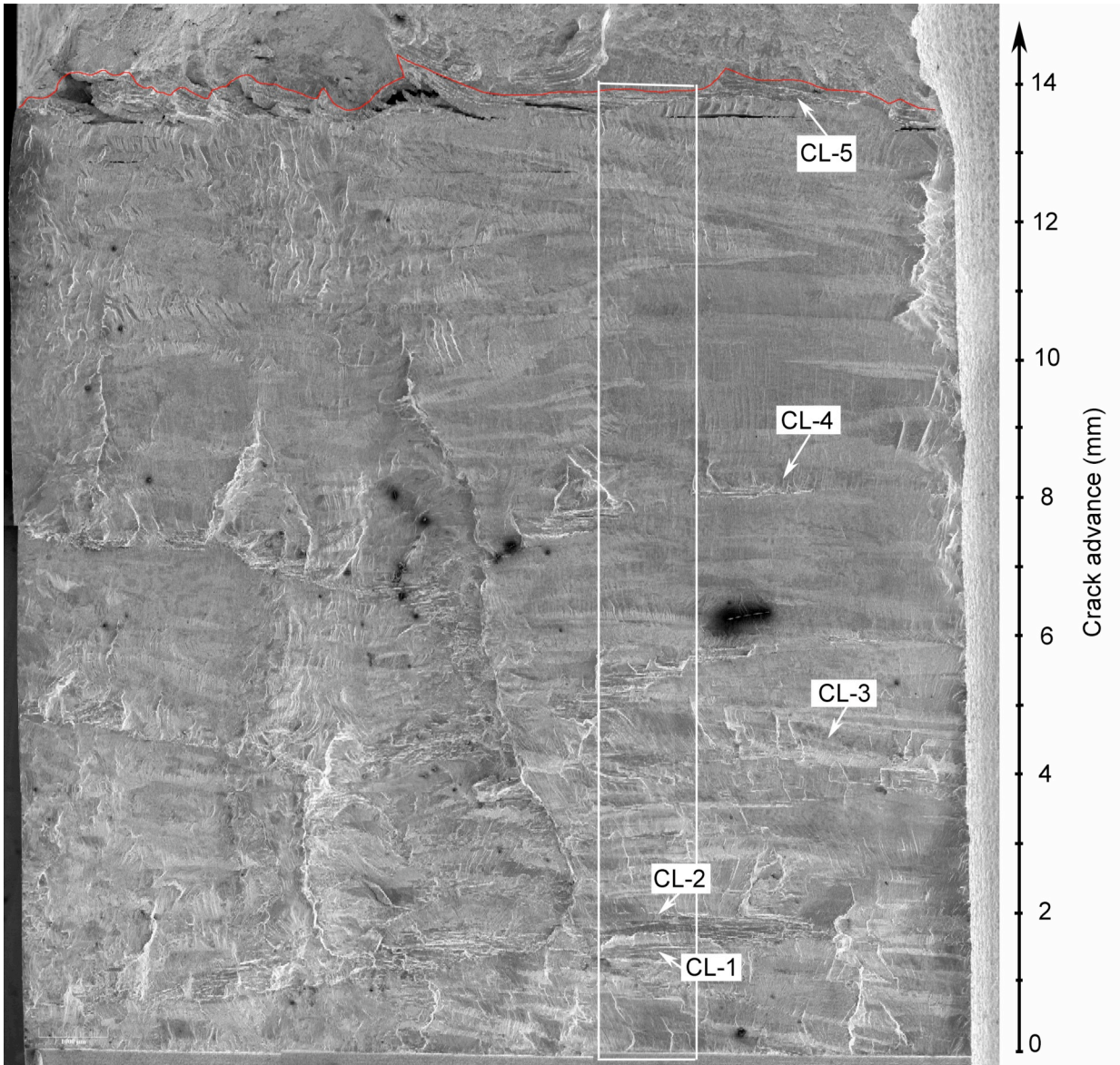
Figure 42. Fracture surface of Alloy 182 weld specimen CT933-TL. The regions dominated by IG fracture corresponding to the constant load (CL) periods are indicated in the figure. The different IG regions are indicated.
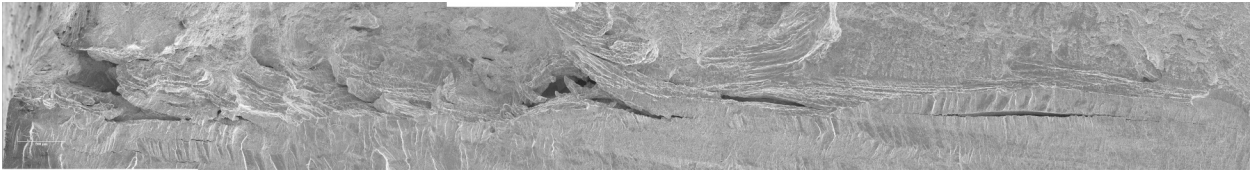

Figure 43. Intergranular fracture on the Alloy 182 weld specimen CT933-TL resulting from the constant–load period CL-5 (test period 20).
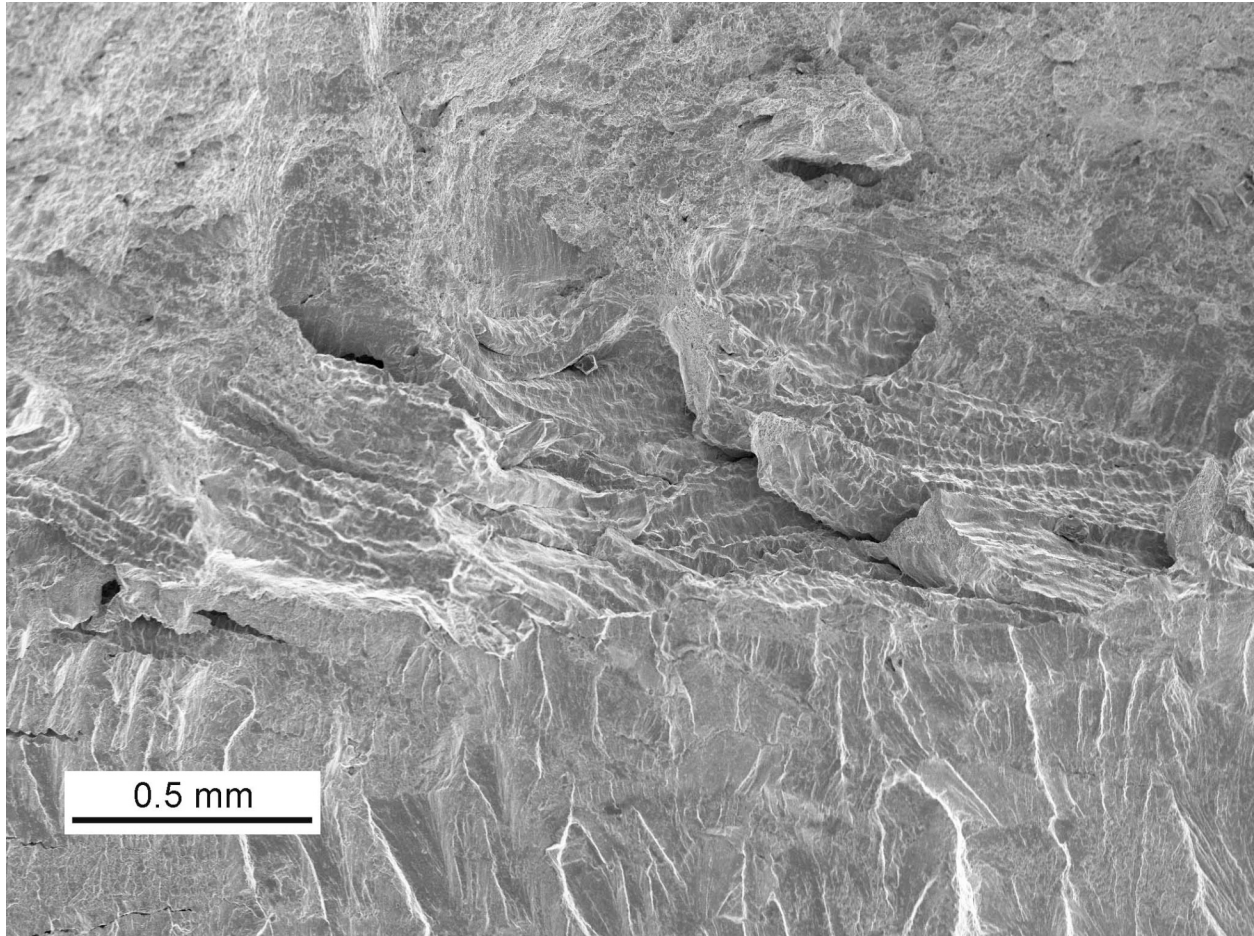
47

Figure 44. Higher magnification image of IG fracture on the Alloy 182 weld specimen CT933-TL resulting from the constant load period CL-5 (test period 20). Crack extension from bottom to top of the figure.

### 4.1.5 Crack Growth Data for Deep-Groove Weld Specimen CT933-LS

A CGR test was conducted on a deep–groove–filled weld specimen in the LS orientation (Specimen CT933-LS). The specimen had to be thinned by approximately 3 mm on each side to ensure that the entire crack front (anticipated to extend 15 mm) will be exclusively in the weld alloy. Prior to the test, the ECPs of a Pt electrode and a companion Alloy 600 electrode downstream from the autoclave were −650 and −690 mV (SHE), respectively. The experimental conditions and results are shown in Table 9, and the changes in crack length and K_{max} with time are shown in Fig. 45. The sample was fatigue precracked at $K_{max} = 24$ MPa m$^{1/2}$, R = 0.3, and a triangular waveform. Next, the specimen was cycled at R = 0.5 at increasing rise times of 50 and 500 s. The system was then set at constant load at $K_{max} = 28$ MPa m$^{1/2}$, followed by constant load at $K_{max} = 40$ MPa m$^{1/2}$. One observes that in Fig. 45b the CGR was determined by connecting the initial crack length at the start of test period 3 and the crack length at the start of the next test period at $K = 40.5$ MPa m$^{1/2}$ (given by the dotted line). The assumption was that the unbroken ligaments snapped when the increased load was applied (note the sudden jump in crack length in Fig. 45b). A similar approach was undertaken for the next constant load period (Fig. 45c).

Table 9. Crack growth data for specimen CT933-LS of Alloy 82 SMA weld in PWR water[a] at 320°C.

Test Period	Test Time, h	Cond.,[b] µS/cm	O_2 Conc.,[b] ppb	Load Ratio R	Rise Time, s	Down Time, s	Hold Time, s	K_{max}, MPa·m$^{1/2}$	ΔK, MPa·m$^{1/2}$	CGR_{env}, m/s	Estimated CGR_{air}, m/s	Crack Length, mm
Pre a	79	26	<10	0.30	0.5	0.5	0	23.71	16.59	1.63E-08	3.42E-08	13.306
Pre b	91	26	<10	0.30	5	5	0	25.88	18.12	7.87E-08	4.87E-09	15.051
Pre c	97	26	<10	0.30	5	5	0	28.49	19.94	1.28E-07	7.22E-09	16.952
1	162	26	<10	0.50	50	2	0	27.67	13.84	3.69E-09	2.77E-10	17.816
2	217	26	<10	0.50	500	12	0	27.91	13.96	7.63E-10	2.88E-11	18.007
3	836	26	<10	1.00	-	-	-	28.73	0.00	1.73E-10	-	18.373
4	1665	26	<10	1.00	-	-	-	44.81	0.00	6.54E-10	-	20.338
5	1690	26	<10	0.5	500	12	0	46.66	23.33	3.69E-09	2.36E-10	21.212

[a]Simulated PWR water with 2 ppm Li, 1100 ppm B, and 2 ppm dissolved hydrogen (≈23 cc/kg).
[b]Represents values in the effluent.
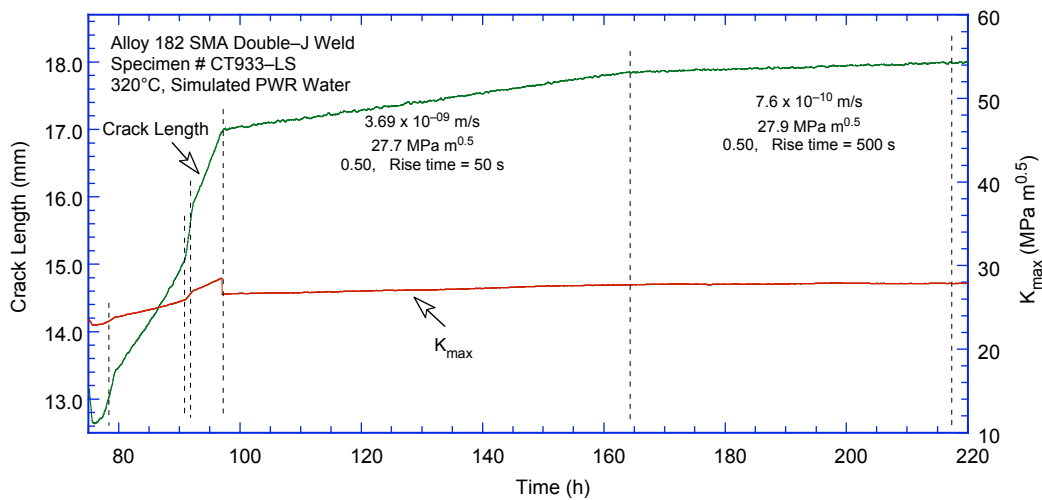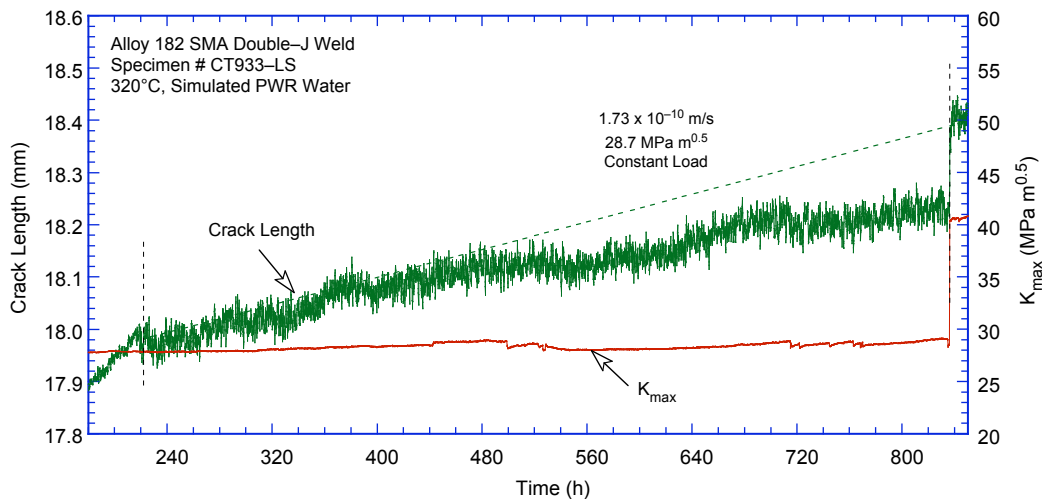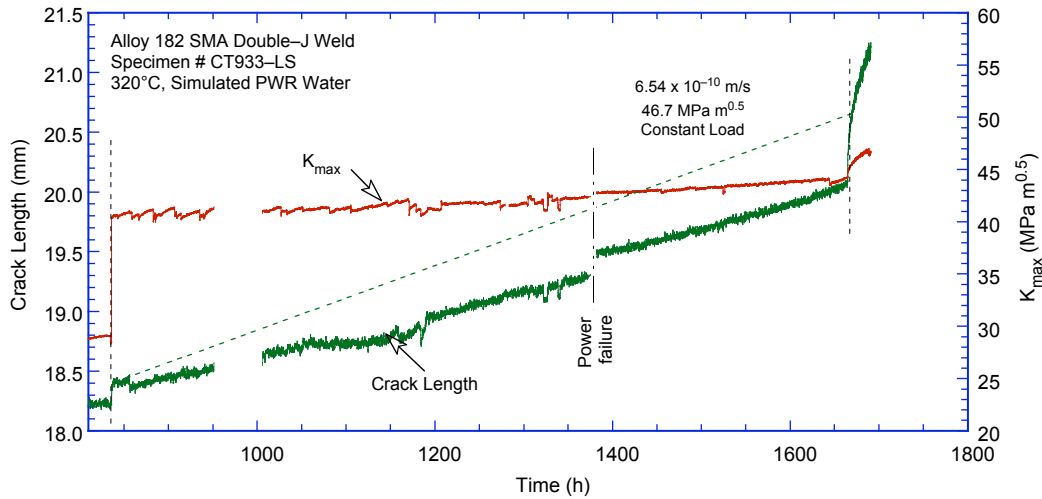

Figure 45. Crack length vs. time for Alloy 182 weld specimen CT933-LS in simulated PWR environment at 320°C during (a) precracking and periods 1-2, (b) constant load period 3, and (c) constant–load period 4.
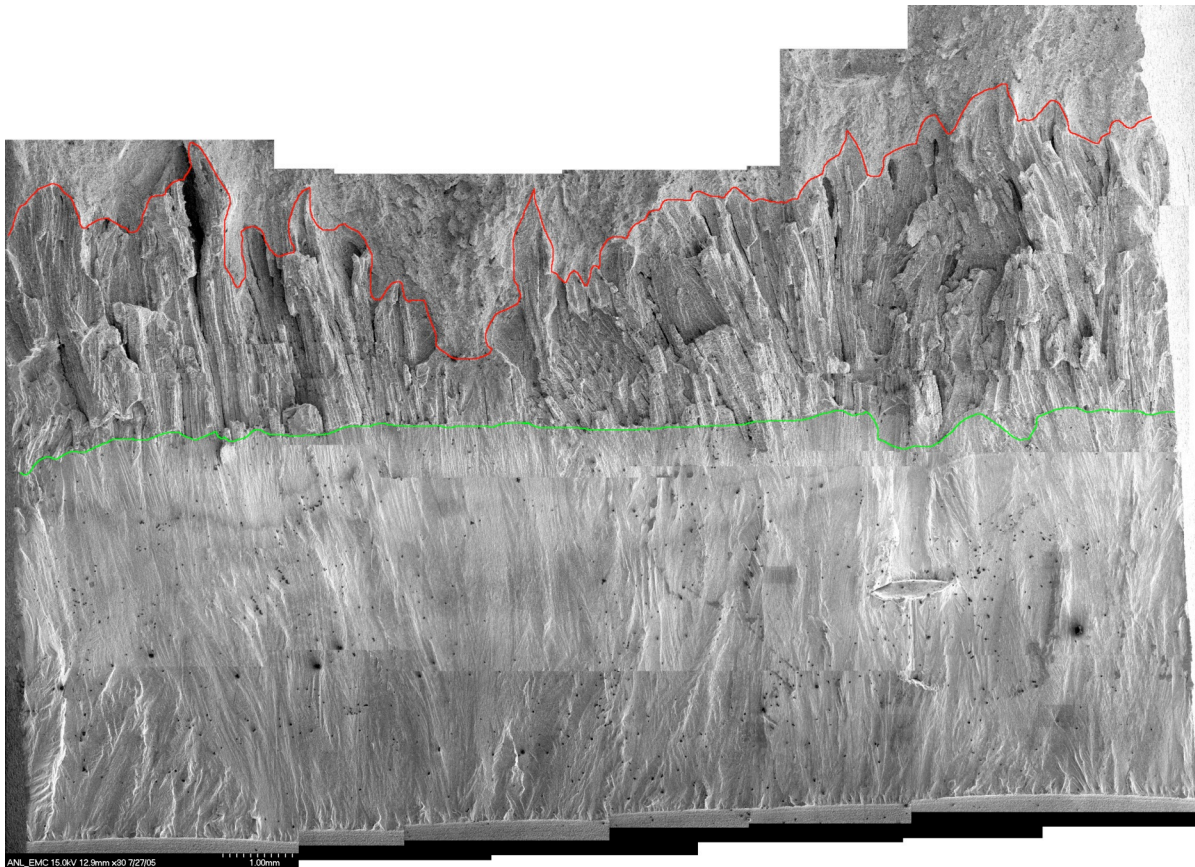
Figure 45　　　(Contd.)

Figure 46.　Crack front on fracture surface of sample CT933-LS. Crack extension from bottom to top of the figure.

Figure 46 shows the entire fracture surface of this specimen. Following pre-cracking the fracture turned into a intergranular mode (IG). Nevertheless, we observe that the testing procedure resulted in a relatively straight crack front. The average crack extension for the transgranular region and the total crack advance were determined by taking ≈20 measurements across the width of the specimen. The

measured total crack extension was greater than the value determined from the DC potential measurements, most likely due to unbroken ligaments in the intergranular region. The DC potential data for the transgranular region was found to be in good agreement with the direct measurements. The intergranular DC potential data was scaled proportionally by a factor 2.30; the corrected data are given in Table 7.

Figure 47 focuses on the transition from TG to IG on the fracture surface of specimen CT933-LS. One observes that following the TG region, elements of IG fracture appear on the fracture surface, most likely during long rise time fatigue periods. Upon transitioning to constant load, the fracture mode changes completely to IG.
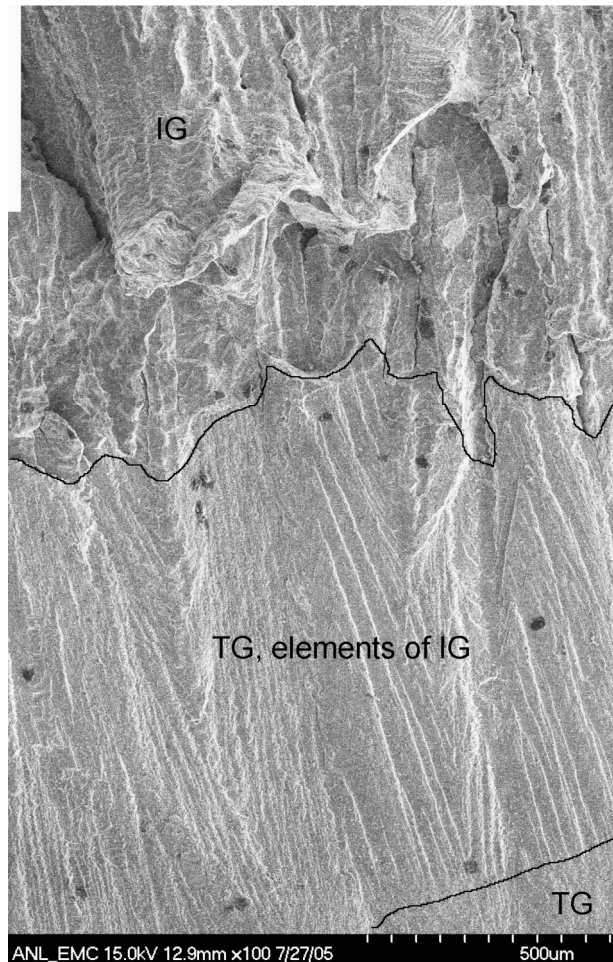

Figure 47.   Transition from TG to IG observed on the fracture surface of sample CT933-LS. Crack extension is from bottom to top of the figure.

4.2 Effect of Grain Boundary Type and Relative Grain Orientation on Crack Propagation

Several studies have been conducted on the effect of grain boundary type (primarily misorientation) on the cracking behavior of Ni-base alloys in primary water environments. Although there appears to be a consensus on the improved resistance to SCC initiation of CSLBs,[32–35,37,38] the effect of such boundaries on SCC propagation is not well understood. Palumbo et al.[32,37,38] have shown that, in Ni-

base alloys, cracking occurs almost exclusively along random interfaces. Similar behavior was reported by Gertsman and Bruemmer[39] for Alloy 600 and by Pan et al.[40] for Alloy X-750. In addition to the experimental observations, quite a few modeling studies have been conducted, based primarily on percolation stochastic methods[41,42] or on concepts such as "grain boundary connectivity"[43] that attempt to explain the effect of grain boundary type on crack propagation. Although it is not clear whether models based on either method fully explain the available crack growth data, they all appear to have one common premise: that cracking will propagate along the HABs.

The objective of this work was to determine whether a propagating stress corrosion crack in weld Alloy 182 is influenced by the character of the grain boundaries it encounters and by the relative orientation of the adjacent grains. Our previous OIM characterization of the Alloy 182 weld alloys currently used in our CGR experiments has shown these weld alloys to have a much higher proportion of SCC-susceptible boundaries (about 75%) than typical solution-annealed Alloy 600 (about 50%). In addition, the OIM data reported previously has shown that, unlike the isotropic Alloy 600, in the weld alloys clusters of grains with similar orientations were observed in the weld microstructure. We hypothesize that a boundary with a weak Taylor factor mismatch – as would be the case for two neighboring grains sharing a similar orientation – would be less susceptible to deformation, thus less susceptible to cracking.[44] The following experiment was conducted to test this hypothesis.
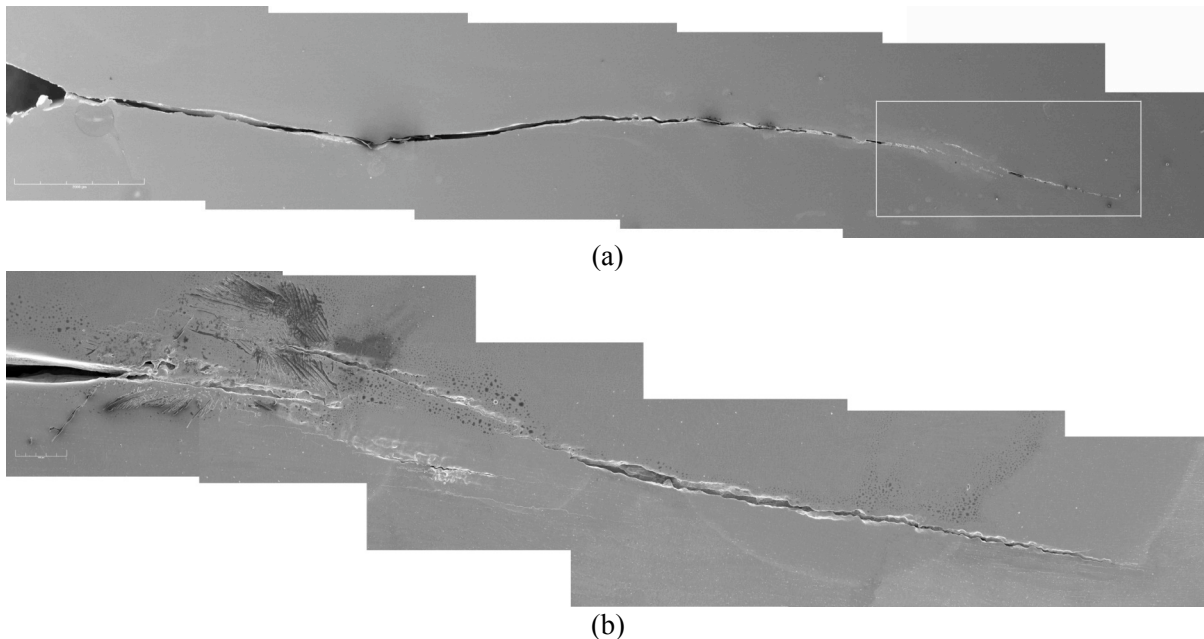

(a)

(b)

Figure 48.   (a) Cross section and (b) SCC area of CT31-W02 TS (boxed region in (a)).

To determine whether the cracking behavior of a grain boundary is influenced by the relative orientation of the adjacent grains, OIM maps were acquired on the cross sections, along the crack path of two specimens, CT31-W02 TS (deep-groove weld) and CT933-TS (double-J weld), from the SCC regions. For specimen CT31-W02 TS the OIM scan was conducted in the boxed area of Fig. 48a, shown at higher magnification in Fig. 48b. By comparing the SEM images with the resulting OIM scans, the characters and the relative orientations of the neighboring grains were recorded for each cracked grain boundary. The cross section of CT933-TS was further cut into three slices, and each slice was scanned separately to improve the cracked boundary statistics. For the OIM analysis, all the specimens were mechanically polished with 1–μm diamond paste and electro-polished in a perchloric acid (10%) and methanol solution at −50°C. The OIM characterization was performed in a Philips XL30 FEG SEM

equipped with a TexSem OIM system. For the subsequent SEM examination of the OIM-scanned areas, in an effort to reveal the finer cracks, too, the samples were etched in a phosphoric acid solution. Figure 49 shows an SEM image of the cross section of CT31-W02 tilted by 70° for OIM analysis. This was taken in the SCC region near the end of the crack.
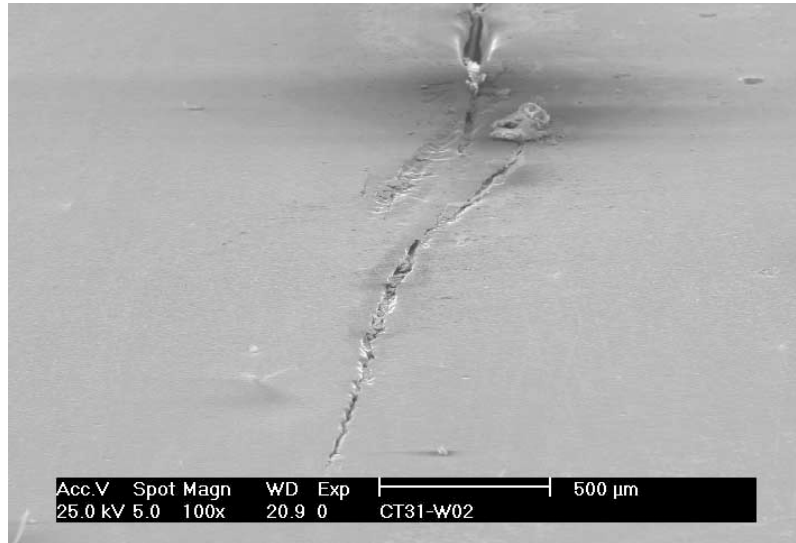

Figure 49.   SEM image of the cross section of CT31-W02 tilted by 70° for OIM analysis.
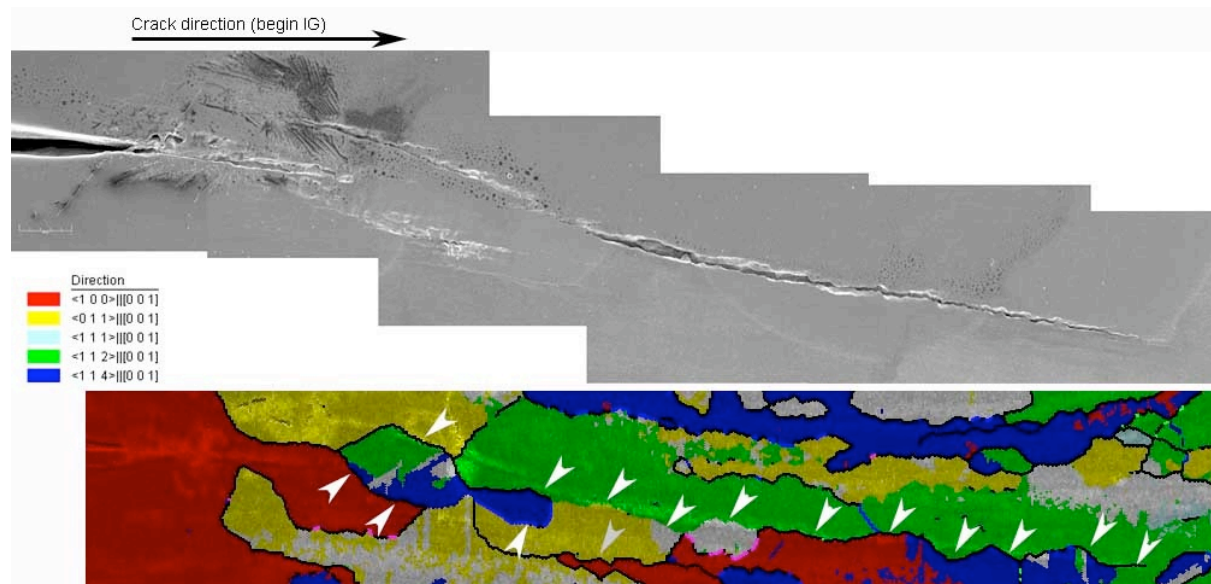

Figure 50.   SCC region of specimen CT31-W02 and resulting OIM map. The cracked boundaries are indicated by arrows on the OIM map.

Figure 50 shows the SEM image of the SCC region of specimen CT31-W02 TS and the resulting OIM map. The cracked boundaries are indicated by arrows on the OIM map. One observes that cracking propagated mostly along HAB, as expected, and mostly along grain boundaries separating grains of different orientations (shown with different colors in the OIM map of Fig. 50). Similarly, Fig. 51 shows the SEM images of the cross sections of the three samples from CT933-TS tilted by 70° for the OIM analysis.
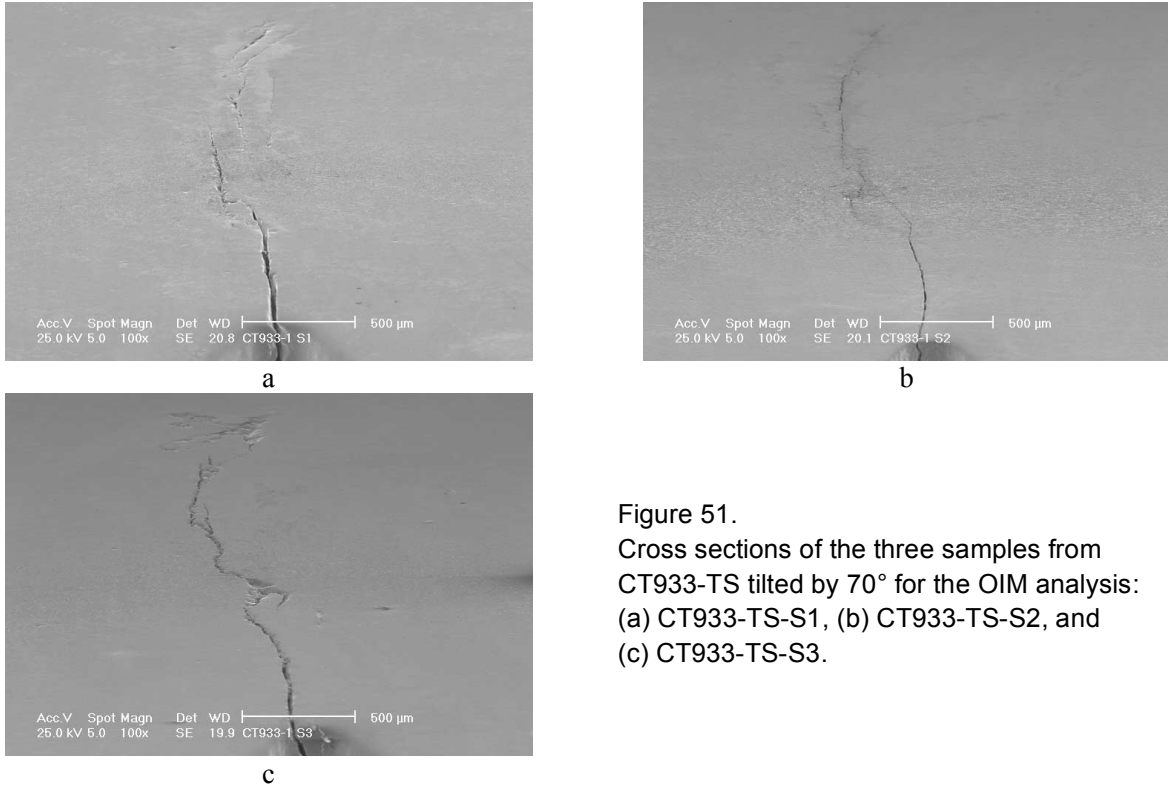
a

b

c

Figure 51.
Cross sections of the three samples from
CT933-TS tilted by 70° for the OIM analysis:
(a) CT933-TS-S1, (b) CT933-TS-S2, and
(c) CT933-TS-S3.

In a similar fashion with CT31-W02 TS, OIM maps were obtained from the SCC regions, and the cracked boundaries were identified in each scan with white arrows, shown in Fig. 52. As in the previous sample, cracking propagated mostly along HABs, and along grain boundaries separating grains of similar orientation.
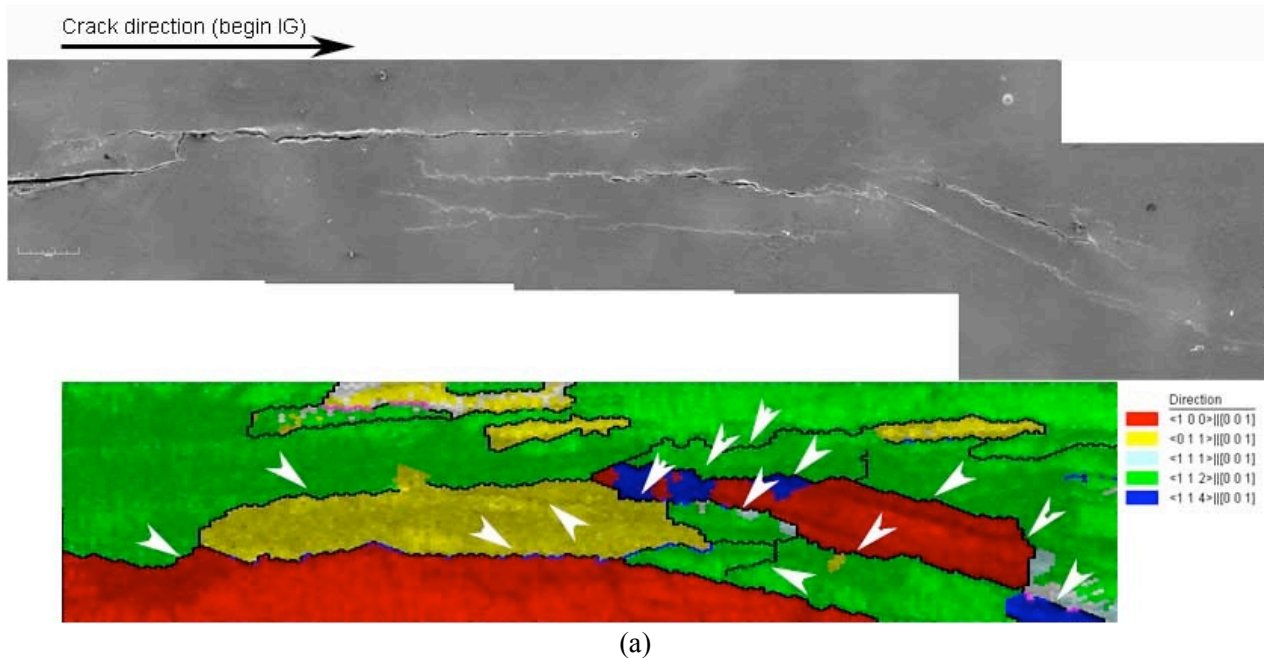

(a)

Figure 52.   SCC regions and resulting OIM map for (a) CT933-TS-S1, (b) CT933-TS-S2, and (c) CT933-TS-S3. The cracked boundaries are indicated by arrows on the OIM map.
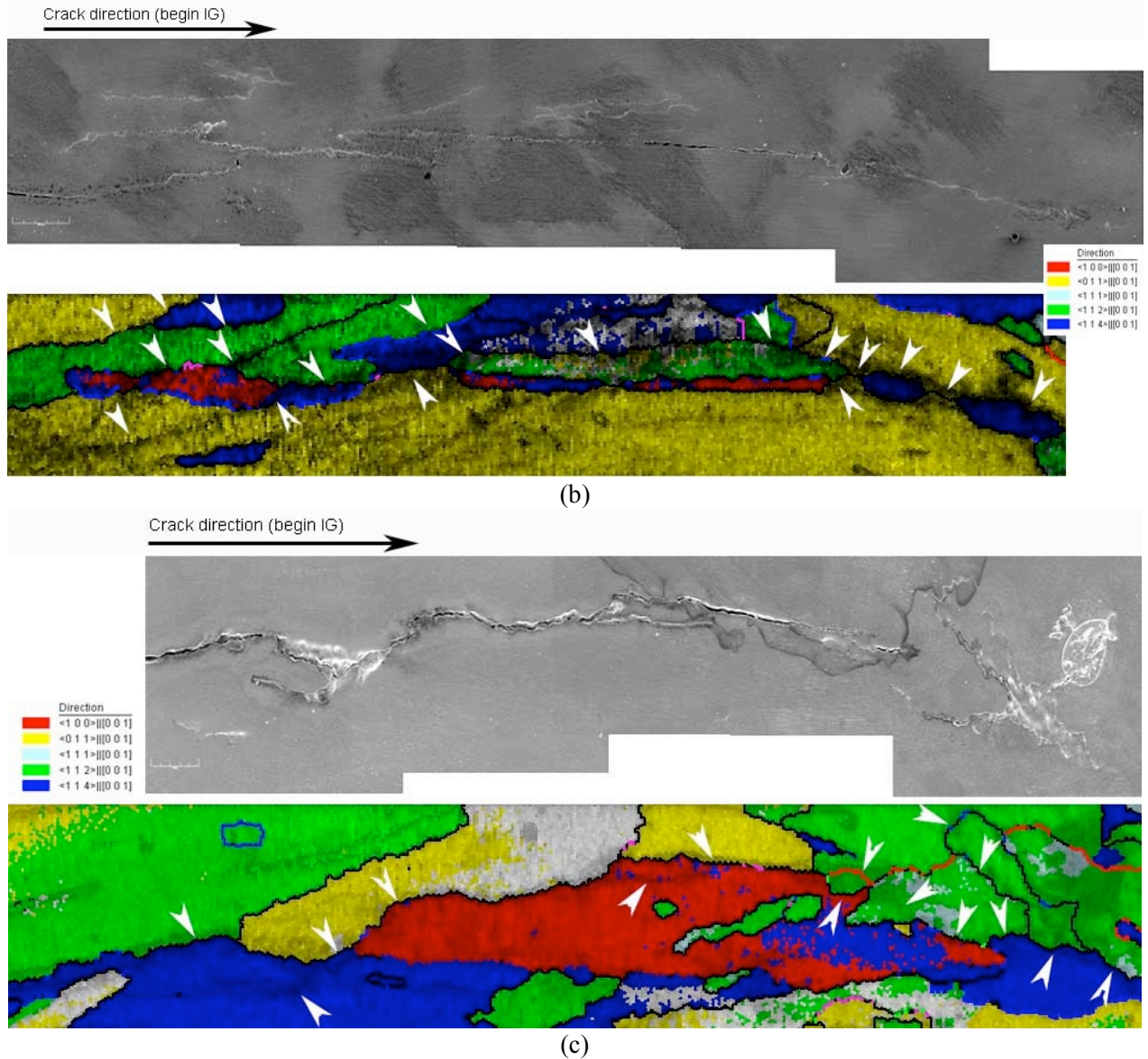
54

(b)

(c)

Figure 52.   (Contd.)

The resulting cracking data, broken down by the orientation of adjacent grains and grain boundary (GB) types for both specimens (all four OIM scans), are shown in Table 10.

Table 10. Cracking data for both CT933-01 and CT31-W02 (all four OIM scans).

Specimen	Total cracked GBs	Orientation of adjacent grains		GB type	
		Different	Similar	HAB	CSLB
CT933-01-S1	14	13	1	13	1
CT933-01-S1	19	16	3	18	1
CT933-01-S1	15	10	5	14	1
Total CT933-01	**48**	**39**	**9**	**45**	**3**
CT31-W02	**15**	**14**	**1**	**13**	**1**

55

Using the data in Table 10, the fractions of cracked boundaries were calculated as a function of boundary type for both specimens. The results are plotted in Fig. 53. The uncertainties in the fractions of cracked boundaries σ_p were calculated according to:

$$\frac{\sigma_p}{p} = \sqrt{\frac{1}{N}\frac{(1-p)}{p}} \,,$$

where p is the fraction of cracked boundaries, and N is the population of boundaries based on which the analysis was made.[45] The fact that a crack is more likely to propagate along HABs was somewhat expected, in light of the numerous studies concluding that crack initiation is more likely to occur at HABs than at CSLBs.[37,35] This result is in very good agreement with results reported by Gertsman and Bruemmer,[39] who found that, in Alloy 600, ≈90 % of the cracked boundaries along a crack path were HABs. Although these authors attributed the increased resistance of the CSLBs to cracking to the relatively high proportions of cracking-immune coherent twins, in the present study, the microstructure does not appear to contain a significant population of twins (see the grain boundary character distribution for welds in Fig. 26). The present results suggest that the CSLBs other than the coherent Σ3s must be more resistant to cracking.
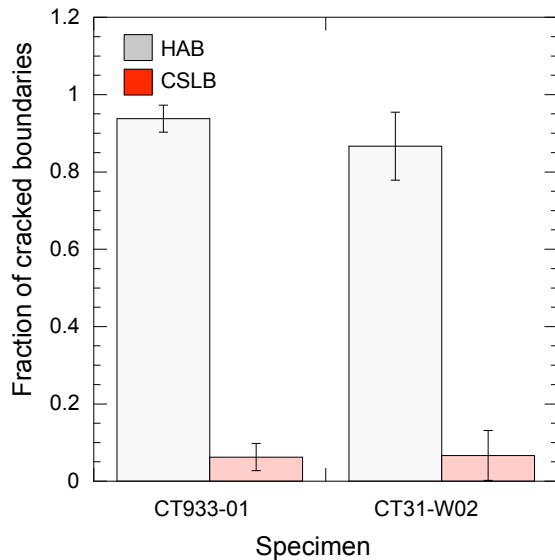

Figure 53.
Fractions of cracked boundaries as a function of boundary type.

The fraction of cracked boundaries is plotted as a function of the relative orientation of the adjacent grains for both specimens in Fig. 54. The bars indicate that grain boundaries that separate grains with similar orientation are more resistant to cracking than boundaries that separate grains with different orientations. That is, the clustering of grains with similar orientations in weld alloys leads to a different class of random (HAB) boundaries, more resistant to SCC than "regular" HABs. This result is in very good agreement with that of Wright and Field for fatigue cracking in a Ni-base superalloy.[46] The authors examined an otherwise-rare cracked Σ3 and found a strong mismatch in Taylor factors across the boundary. Based on this finding, the authors suggested that Taylor factors should be included in the description of a grain boundary.
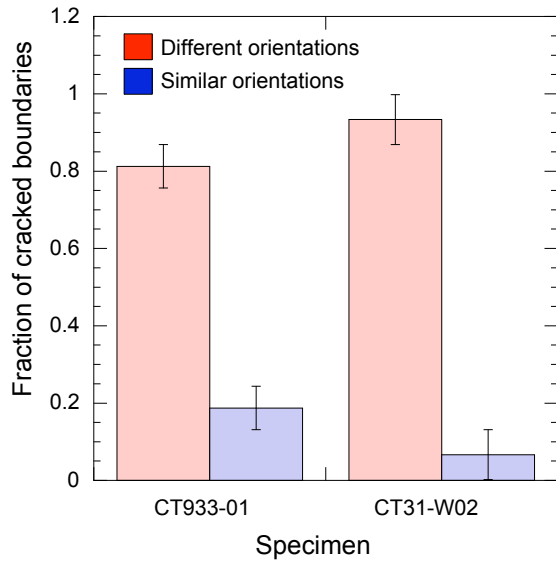
Figure 54.
Fractions of cracked boundaries as a function of the relative orientation of the adjacent grains.

Therefore, while the weld Alloy 182 contains a significantly lower CSLB fraction than a typical Alloy 600, these may not necessarily control the cracking behavior of the weld alloys. The microstructure of Alloy 182 contains clusters of grains with similar orientations, and these were found to be more resistant to cracking than boundaries that separate grains of different orientations; therefore, this information should be included along with misorientation for a better description of an alloy's susceptibility to SCC.